



**HAL**  
open science

# Limiting amplitude principle and resonances in plasmonic structures with corners: numerical investigation

Camille Carvalho, Patrick Ciarlet, Claire Scheid

► **To cite this version:**

Camille Carvalho, Patrick Ciarlet, Claire Scheid. Limiting amplitude principle and resonances in plasmonic structures with corners: numerical investigation. *Computer Methods in Applied Mechanics and Engineering*, 2022, 388, pp.114207. 10.1016/j.cma.2021.114207 . hal-03160574v2

**HAL Id: hal-03160574**

**<https://hal.science/hal-03160574v2>**

Submitted on 25 Oct 2021

**HAL** is a multi-disciplinary open access archive for the deposit and dissemination of scientific research documents, whether they are published or not. The documents may come from teaching and research institutions in France or abroad, or from public or private research centers.

L'archive ouverte pluridisciplinaire **HAL**, est destinée au dépôt et à la diffusion de documents scientifiques de niveau recherche, publiés ou non, émanant des établissements d'enseignement et de recherche français ou étrangers, des laboratoires publics ou privés.

# Limiting amplitude principle and resonances in plasmonic structures with corners: numerical investigation

Camille Carvalho<sup>a,\*</sup>, Patrick Ciarlet Jr.<sup>b</sup>, Claire Scheid<sup>c</sup>

<sup>a</sup>*Applied Math Department, University of California Merced, 5200 N Lake Rd, Merced, CA 95348, United-States*

<sup>b</sup>*POEMS, CNRS, INRIA, ENSTA Paris, Institut Polytechnique de Paris, 91120 Palaiseau, France*

<sup>c</sup>*Université Côte d'Azur, LJAD, CNRS, INRIA, 06103 Nice, France*

---

## Abstract

The limiting amplitude principle states that the response of a scatterer to a harmonic light excitation is asymptotically harmonic with the same pulsation. Depending on the geometry and nature of the scatterer, there might or might not be an established theoretical proof validating this principle. In this paper, we investigate a case where the theory is missing: we consider a two-dimensional dispersive Drude structure with corners. In the non lossy case, it is well known that looking for harmonic solutions leads to an ill-posed problem for a specific range of critical pulsations, characterized by the metal's properties and the aperture of the corners. Ill-posedness is then due to highly oscillatory resonances at the corners called black-hole waves. However, a time-domain formulation with a harmonic excitation is always mathematically valid. Based on this observation, we conjecture that the limiting amplitude principle might not hold for all pulsations. Using a time-domain setting, we propose a systematic numerical approach that allows to give numerical evidences of the latter conjecture, and find clear signature of the critical pulsations. Furthermore, we connect our results to the underlying physical plasmonic resonances that occur in the lossy physical metallic case.

*Keywords:* Limiting amplitude principle, Plasmonics, Black-hole waves

---

## 1. Introduction

Plasmonic structures are commonly made of noble metals (silver, gold, etc.) and dielectrics (air, vacuum, glass). At optical frequencies, metals can be dispersive, allowing the propagation of localized surface waves at the metal-dielectric interface called surface plasmons [1]. The field of plasmonics is very active as surface plasmons offer strong light enhancement, with applications to next-generation sensors, antennas, high-resolution imaging, cloaking and other [2, 3, 4, 5, 6, 7]. Several models are available in the literature to model dispersive materials. In particular, Drude model [8] is relevant for classical noble materials: in this approximation, the metal is considered as a free electrons gas (with a static lattice of positive ions). Then interactions of these electrons with the ion lattice manifest through a collision frequency parameter, representing dissipation

---

\*Email address: ccarvalho3@ucmerced.edu

11 in the equations. Over the past decades, new models have been developed, including the so-  
12 called negative-index metamaterial, and interesting ideal cases (negligible dissipation) have been  
13 uncovered.

14 If the source of incident illumination is monochromatic, one would naturally expect the time  
15 dependent electromagnetic field to evolve asymptotically (in time) to a harmonic state with the  
16 corresponding incident frequency. This asymptotic harmonic behavior is called *Limiting ampli-*  
17 *tude principle* and allows to work with the associated frequency-domain boundary value problem.  
18 The limiting amplitude principle has been investigated for a long time, and is well understood  
19 for the wave equation and related classical scattering problems [9, 10, 11, 12, 13]. Recently there  
20 has been a new interest in exploring this principle in the context of emerging plasmonic struc-  
21 tures [14, 15]. In particular, the specific case of a planar interface with a non lossy Lorentz model  
22 has been fully investigated in [15]. However for other configurations, the landscape is different:  
23 this is especially not clear for (non lossy) plasmonic structures with corners.

24 The limiting amplitude principle is closely related to well-posedness of the corresponding  
25 harmonic equation. Although the time-dependent equations system is mathematically well-posed  
26 (in the usual function spaces), the frequency-domain counterpart has proven to be more challeng-  
27 ing [16, 17, 18, 19, 20, 21, 22]. A key point lies in the fact that the Fourier transform of a non  
28 lossy metal's constitutive law can correspond to a real negative permittivity<sup>1</sup>. The induced possi-  
29 ble change of sign of the permittivity at the interface affects the optical response. If the structure  
30 has corners, the frequency-domain equations system may be mathematically ill-posed for a range  
31 of critical frequencies (corresponding to a critical range of permittivities). In this range of fre-  
32 quencies, hypersingular behaviors arise at the interface (especially at corners), requiring specific  
33 numerical treatments to avoid spurious reflections and inaccurate predictions. Ill-posedness in  
34 frequency-domain corresponds to an unphysical *infinite* electromagnetic energy, indicating that  
35 *the limiting amplitude principle should not hold in that case*. This conjecture motivates our  
36 exploration.

37 In this paper we provide a systematic approach to numerically assess the latter conjecture  
38 in non lossy subwavelength plasmonic structures with corners. We base our strategy on a time-  
39 domain framework. From typical quantities of interest (fields, energy, cross sections, Poynt-  
40 ing flux, etc.), we manage to identify a signature of the underlying critical interval from the  
41 frequency-domain, by using time-domain simulations. Our results show a clear change of be-  
42 havior at critical frequencies. Additionally, we find this signature also when considering physical  
43 structures (incorporating losses): in other words the limit non lossy case is useful to highlight  
44 intrinsic resonances in physical plasmonic structures.

45 The paper is organized as follows. Section 2 presents the general context, the model problem  
46 along with relevant quantities of interest. In Section 3, we specify the two-dimensional (or 2D),  
47 geometrical, physical and numerical framework that we precisely consider to explore the limiting  
48 amplitude principle. The numerical evidences that assess our conjecture are detailed in Section 4.  
49 Then, in Section 5, we continue our efforts towards a more physical discussion. Finally Section  
50 6 presents our concluding remarks.

## 51 **2. General context: plasmonics and limiting amplitude principle**

### 52 *2.1. Drude Model in plasmonics*

53 As mentioned in the introduction, plasmonic structures are commonly made of noble metals

---

<sup>1</sup>It commonly provides some imaginary part for lossy materials.

54 and dielectrics, where surface plasmons arise at the interface at optical frequencies. We present  
 55 below the well-known Drude model and related equations to model the electromagnetic field in  
 56 those structures.

57 Metals at optical frequencies are known to be dispersive: each monochromatic wave trav-  
 58 els with different speeds through the metallic material. To accurately model optical properties of  
 59 metallic structures, one has thus to rely on models that take into account the frequency-dependent  
 60 velocity of the wave. This dispersion phenomenon is equivalently explained as a delay effect in  
 61 the reaction of the electrons of the metal to light excitation. In this work, we will use the well-  
 62 known Drude model to account for this dispersion phenomenon. It is based on the kinetic theory  
 63 of gases [8], considering the metal as a static lattice of positive ions immersed in a free electrons  
 64 gas. In the case of scattering by a metallic obstacle, the set of (linearized) equations can be even-  
 65 tually summarized as follows.

66 The time-dependent electromagnetic field is computed using time-domain Maxwell's equations  
 67 with variables  $(\mathbf{D}, \mathbf{E}, \mathbf{B}, \mathbf{H})^2$  where dispersive effects are incorporated through the electric consti-  
 68 tutive law. The latter relates the electric displacement  $\mathbf{D}$  and the electric field  $\mathbf{E}$  and incorporates  
 69 the possible time history (when dispersive effects are taken into account) via a time convolution  
 70 (denoted  $*_t$ ):

$$\mathbf{D} = \varepsilon *_t \mathbf{E}, \quad (1)$$

71 where

$$\varepsilon(t, \cdot) := \delta_0(t) \varepsilon_0 \varepsilon_r(\cdot) + \chi(t, \cdot), \quad (2)$$

72 is the space-time dielectric permittivity,  $\varepsilon_0$  the vacuum permittivity,  $\varepsilon_r$  the relative permittivity  
 73 and  $\chi$  is the electric sensitivity. These quantities are defined in  $\mathbb{R}^3$  and such that causality property  
 74 holds (see *e.g.* [23] for a nice review). Since we do not take any dispersive effects into account in  
 75 the dielectric, one sets  $\chi = 0$  there. However, in the metallic obstacle,  $\chi$  is non vanishing. If one  
 76 defines the polarization current  $\mathbf{J}$  as  $\mathbf{J} := -\partial_t(\chi *_t \mathbf{E})$ , one can rewrite the whole set of Maxwell's  
 77 equations in terms of  $(\mathbf{E}, \mathbf{H}, \mathbf{J})$  variables only. In particular,  $\mathbf{J}$  verifies a linear differential equation  
 78 that is linearly coupled to  $(\mathbf{E}, \mathbf{H})$  through classical Maxwell's equations. With this approach, we  
 79 do not need the expression of  $\chi$  explicitly. The reason is that Drude model is entirely determined  
 80 via the variable  $\mathbf{J}$  (see below). We will see later that  $\chi$  plays an important role in frequency-  
 81 domain.

82 We fix an *end time*  $T > 0$ , and a *domain*  $\Omega$ , that is an open and connected subset of  $\mathbb{R}^3$  with  
 83 Lipschitz boundary. In our model, the domain  $\Omega$  is the metallic obstacle, and it is immersed in  
 84 a homogeneous dielectric background. For the practical choice of the end time  $T$  in numerical  
 85 simulations, we refer to subsection 3.4. In what follows,  $\mu_0$  denotes the permeability of vacuum,  
 86  $\varepsilon_d$  denotes the dielectric relative permittivity of the dielectric and  $\varepsilon_\infty$  the relative permittivity (at  
 87 infinite frequency) of the metallic obstacle  $\Omega$ . We now set

$$\varepsilon_r(\mathbf{x}) := \begin{cases} \varepsilon_d, & \text{for } \mathbf{x} \in \mathbb{R}^3 \setminus \bar{\Omega}, \\ \varepsilon_\infty, & \text{for } \mathbf{x} \in \Omega, \end{cases} \quad (3)$$

---

<sup>2</sup>respectively electric displacement, electric field, magnetic induction, magnetic field.

88 and we will denote  $\varepsilon := \varepsilon_0 \varepsilon_r$ . Thereafter, Drude model in the time-domain writes on  $[0, T]$  as:

$$\mu_0 \frac{\partial \mathbf{H}}{\partial t} = -\mathbf{curl} \mathbf{E} \text{ in } \mathbb{R}^3, \quad (4a)$$

$$\varepsilon_0 \varepsilon_d \frac{\partial \mathbf{E}}{\partial t} = \mathbf{curl} \mathbf{H} + \mathbf{J}_{ext} \text{ in } \mathbb{R}^3 \setminus \bar{\Omega}, \quad (4b)$$

$$\varepsilon_0 \varepsilon_\infty \frac{\partial \mathbf{E}}{\partial t} = \mathbf{curl} \mathbf{H} - \mathbf{J} + \mathbf{J}_{ext} \text{ in } \Omega, \quad (4c)$$

$$\frac{\partial \mathbf{J}}{\partial t} = \omega_p^2 \varepsilon_0 \mathbf{E} - \gamma \mathbf{J} \text{ in } \Omega, \quad (4d)$$

$$\mathbf{J} = 0, \text{ in } \mathbb{R}^3 \setminus \bar{\Omega}, \quad (4e)$$

89 where  $\omega_p$  is the plasma angular frequency, and  $\gamma$  the collision frequency (coming from Drude  
90 model). Here  $\mathbf{J}_{ext}$  denotes a possible external current that we will use to model volumic source  
91 excitation in the following.

92 **Remark 1.** *Note that the plasma angular frequency characterizes the angular frequency above*  
93 *which an incident wave can completely penetrate the metal. On the other hand, the strong*  
94 *plasmonic effects induced by surface plasmons are obtained by an illumination, below the plasma*  
95 *angular frequency, of subwavelength metallic structures.*

96 We will call this system *time-dependent Maxwell-Drude equations in plasmonic structures.*

97 *Well-posedness.* As commonly done, in order to compute the solution, we will artificially truncate  
98 the *exterior domain*  $\mathbb{R}^3 \setminus \bar{\Omega}$  and close the system (4) by adding approximate transparent  
99 boundary conditions (for  $\mathbf{E}$  and  $\mathbf{H}$ ), transmission conditions at  $\partial\Omega$  (for  $\mathbf{E}$  and  $\mathbf{H}$ ) and initial  
100 conditions (for  $\mathbf{E}$ ,  $\mathbf{H}$  and  $\mathbf{J}$ ). At the artificial boundary, to approximate transparent boundary  
101 conditions, we will use classical first order Silver-Müller boundary conditions. In this setting,  
102 using classical semi-group theory, one can prove that system (4) is well posed<sup>3</sup> (see e.g. [24] for  
103 details).

104 *Excitation.* Several excitations of the scatterer are possible. A physically compliant one consists  
105 of using an incident illumination that we denote  $(\mathbf{E}_{inc}, \mathbf{H}_{inc})$ . To take this illumination into account  
106 in the set of equations, we use the non homogeneous Silver-Müller boundary conditions  
107 as:

$$\mathbf{n} \times \mathbf{E} - \mathbf{n} \times \left( \sqrt{\frac{\mu_0}{\varepsilon_0}} \mathbf{H} \times \mathbf{n} \right) = \mathbf{n} \times \mathbf{g}_{inc}, \quad (5)$$

108 with  $\mathbf{g}_{inc} = \mathbf{E}_{inc} - \left( \sqrt{\frac{\mu_0}{\varepsilon_0}} \mathbf{H}_{inc} \times \mathbf{n} \right)$  and  $\mathbf{n}$  the outward normal to the exterior artificial boundary.

109 **Remark 2.** *As a result, the total electromagnetic field  $(\mathbf{E}, \mathbf{H})$  can be decomposed into an incident*  
110 *contribution  $(\mathbf{E}_{inc}, \mathbf{H}_{inc})$  and a scattered one  $(\mathbf{E}_{sca}, \mathbf{H}_{sca})$ . The scattered field  $(\mathbf{E}_{sca}, \mathbf{H}_{sca})$  verifies*  
111 *Maxwell's equations with homogeneous radiation condition and a source term  $\mathbf{J}_{ext}$ .*

<sup>3</sup>this result is obtained in the natural space  $C^0([0, T], H(\mathbf{curl})) \times C^0([0, T], H(\mathbf{curl})) \times C^0([0, T], L^2)$  with  $L^2$  tangential traces for  $\mathbf{E}$  and  $\mathbf{H}$ .

112 *Electromagnetic energy, Poynting vector.* We define the time-dependent total energy of system  
 113 (4) by

$$\mathcal{E}(t) = \frac{1}{2} \|\sqrt{\varepsilon_0 \varepsilon_r} \mathbf{E}(\cdot, t)\|_{L^2(\mathbb{R}^3)}^2 + \frac{1}{2} \|\sqrt{\mu_0} \mathbf{H}(\cdot, t)\|_{L^2(\mathbb{R}^3)}^2 + \frac{1}{2\varepsilon_0 \omega_p^2} \|\mathbf{J}(\cdot, t)\|_{L^2(\mathbb{R}^3)}^2. \quad (6)$$

114 The space-time dependent Poynting vector also plays a central role in the study of the energy's  
 115 variations, classically defined as

$$\mathbf{\Pi} = \mathbf{E} \times \mathbf{H}. \quad (7)$$

116 Recalling that we have  $\operatorname{div}(\mathbf{E} \times \mathbf{H}) = \mathbf{H} \cdot \operatorname{curl} \mathbf{E} - \mathbf{E} \cdot \operatorname{curl} \mathbf{H}$ , formally we get, using equations (4)

$$\begin{aligned} \frac{\partial \mathcal{E}}{\partial t}(t) &= \int_{\mathbb{R}^3} (\operatorname{div}(\mathbf{E}(\mathbf{x}, t) \times \mathbf{H}(\mathbf{x}, t)) + \mathbf{J}_{ext}(\mathbf{x}, t) \cdot \mathbf{E}(\mathbf{x}, t)) d\mathbf{x} \\ &\quad + \int_{\Omega} \mathbf{J}(\mathbf{x}, t) \cdot \mathbf{E}(\mathbf{x}, t) - \mathbf{E}(\mathbf{x}, t) \cdot \mathbf{J}(\mathbf{x}, t) d\mathbf{x} - \frac{\gamma}{\varepsilon_0 \omega_p^2} \int_{\Omega} \mathbf{J}(\mathbf{x}, t) \cdot \mathbf{J}(\mathbf{x}, t) d\mathbf{x}, \\ &= \int_{\mathbb{R}^3} \operatorname{div}(\mathbf{\Pi}(\mathbf{x}, t)) d\mathbf{x} + \int_{\mathbb{R}^3} \mathbf{J}_{ext}(\mathbf{x}, t) \cdot \mathbf{E}(\mathbf{x}, t) d\mathbf{x} - \frac{\gamma}{\varepsilon_0 \omega_p^2} \int_{\Omega} \mathbf{J}(\mathbf{x}, t) \cdot \mathbf{J}(\mathbf{x}, t) d\mathbf{x}. \end{aligned} \quad (8)$$

117 The pointwise version of the equality is the Poynting theorem. From (8), we deduce that if  
 118  $\mathbf{J}_{ext} \equiv 0$ ,  $\operatorname{div}(\mathbf{\Pi}(\mathbf{x}, t)) \equiv 0$  and  $\gamma = 0$ , then the energy is preserved. If  $\mathbf{J}_{ext} \equiv 0$  and the quantity  
 119  $\operatorname{div}(\mathbf{\Pi}(\mathbf{x}, t)) \leq 0$ , then the energy is dissipated. In the rest of the paper, we focus on the limit case  
 120 where there is no physical dissipation, i.e.  $\gamma = 0$ .

121 **Remark 3.** *When using first order Silver-Müller boundary conditions, we introduce artificial*  
 122 *dissipation in the system and as a result  $\operatorname{div}(\mathbf{\Pi}(\mathbf{x}, t)) \leq 0$  if the condition is homogeneous.*

123 *Long time asymptotics.* If the source is monochromatic, one would naturally expect the solution  
 124 to evolve asymptotically (in time) to a harmonic state with the corresponding incident frequency.  
 125 This asymptotic harmonic behavior is called *Limiting amplitude principle*. This principle holds  
 126 for standard settings and is closely related to well-posedness of the corresponding harmonic  
 127 equation. This principle is well-understood in classic dielectric materials. However in the non  
 128 lossy case and for objects with corners, the landscape is different and less trodden.

## 129 2.2. Limiting amplitude principle

130 The limiting amplitude principle has been studied for a long time (e.g. [9, 10, 11, 12, 13]) and  
 131 states the following. Given a source  $t \mapsto e^{-i\omega t} \mathbf{F}(\cdot)$ , with  $\mathbf{F} \in L^2(\mathbb{R}^3)$  (and support  $\operatorname{supp} \mathbf{F} \Subset \mathbb{R}^3$ ), a  
 132 given pulsation  $\omega > 0$ , and a problem of the form  $\partial_t^2 \mathbf{U} + \mathcal{L} \mathbf{U} = e^{-i\omega t} \mathbf{F}$ , with  $\mathcal{L}$  a linear differential  
 133 operator, then after a long time the solution asymptotically behaves as  $\mathbf{U} = e^{-i\omega t} \mathbf{W}$  with  $\mathbf{W}$   
 134 satisfying a problem of the form  $-\omega^2 \mathbf{W} + \mathcal{L} \mathbf{W} = \mathbf{F}$ .

135 This statement indicates that a periodic regime is asymptotically established and therefore it is  
 136 natural to consider the problem in the time-harmonic regime (stationary problem).

137 Assume for now we can write the external current  $\mathbf{J}_{ext}(\mathbf{x}, t) = \Re(\underline{\mathbf{J}}_{ext}(\mathbf{x}) e^{-i\omega t})$ , and  $(\mathbf{E}, \mathbf{H}, \mathbf{J})(\mathbf{x}, t) =$   
 138  $\Re(\underline{\mathbf{E}}(\mathbf{x}) e^{-i\omega t}, \underline{\mathbf{H}}(\mathbf{x}) e^{-i\omega t}, \underline{\mathbf{J}}(\mathbf{x}) e^{-i\omega t})$ , with  $\underline{\mathbf{J}}_{ext}, \underline{\mathbf{E}}, \underline{\mathbf{H}}, \underline{\mathbf{J}}$  denoting complex-valued fields. Then sys-  
 139 tem (4) (with  $\gamma = 0$ ) simplifies to

$$-i\omega \mu_0 \underline{\mathbf{H}} = -\operatorname{curl} \underline{\mathbf{E}} \quad \text{in } \mathbb{R}^3, \quad (9a)$$

$$-i\omega \varepsilon_0 \hat{\varepsilon}_r \underline{\mathbf{E}} = \operatorname{curl} \underline{\mathbf{H}} + \underline{\mathbf{J}}_{ext} \quad \text{in } \mathbb{R}^3, \quad (9b)$$

140 with

$$\hat{\varepsilon}_r(\mathbf{x}, \omega) := \begin{cases} \varepsilon_d > 0, & \text{for } \mathbf{x} \in \mathbb{R}^3 \setminus \bar{\Omega}, \\ \varepsilon_m(\omega) = \left( \varepsilon_\infty - \frac{\omega_p^2}{\omega^2} \right), & \text{for } \mathbf{x} \in \Omega \end{cases}, \quad (10)$$

141 and transmission conditions, plus some radiation condition at infinity. Indeed,  $\underline{\mathbf{J}}$  is known, and  
 142 equal to  $i \frac{\omega_p^2 \varepsilon_0}{\omega} \underline{\mathbf{E}}$  in  $\Omega$ , respectively 0 in  $\mathbb{R}^3 \setminus \bar{\Omega}$ . We will also denote  $\hat{\varepsilon} := \varepsilon_0 \hat{\varepsilon}_r$ . Above  $\varepsilon_0 \varepsilon_m(\omega)$   
 143 represents the non lossy Drude model permittivity. Let us point out that if  $0 < \omega < \frac{\omega_p}{\sqrt{\varepsilon_\infty}}$  (optical  
 144 frequency range), then  $\varepsilon_m(\omega) < 0$ . System (9) will be called the *frequency-dependent Maxwell-Drude*  
 145 *equations in plasmonic structures*.

147 **Remark 4.** We make the abuse of terminology to denote  $\omega$  by the terms *pulsation, frequency, or*  
 148 *angular frequency*. However in numerical experiments,  $\omega$  will be always given in  $\text{rad.s}^{-1}$ .

149 *Well-posedness.* Classical theory considers  $\underline{\mathbf{E}}, \underline{\mathbf{H}} \in \mathbf{H}_{\text{loc}}(\mathbf{curl}) := \{\mathbf{X} \in L^2_{\text{loc}}(\mathbb{R}^3) \mid \forall \xi \in C_c^\infty(\mathbb{R}^3), \xi \mathbf{X} \in$   
 150  $\mathbf{H}(\mathbf{curl})\}$ , and (9) is equivalent to solve:

$$\mathbf{curl} \hat{\varepsilon}_r^{-1} \mathbf{curl} \underline{\mathbf{H}} - k^2 \underline{\mathbf{H}} = -\mathbf{curl} \hat{\varepsilon}_r^{-1} \underline{\mathbf{J}}_{\text{ext}} \text{ in } \mathbb{R}^3, \quad (11a)$$

$$-i\omega \varepsilon_0 \hat{\varepsilon}_r \underline{\mathbf{E}} = \mathbf{curl} \underline{\mathbf{H}} + \underline{\mathbf{J}}_{\text{ext}} \text{ in } \mathbb{R}^3, \quad (11b)$$

151 with  $k = \omega \sqrt{\varepsilon_0 \mu_0}$ . One can also consider the system

$$-i\omega \mu_0 \underline{\mathbf{H}} = -\mathbf{curl} \underline{\mathbf{E}} \text{ in } \mathbb{R}^3, \quad (12a)$$

$$\mathbf{curl} \mathbf{curl} \underline{\mathbf{E}} - k^2 \hat{\varepsilon}_r \underline{\mathbf{E}} = -i\omega \mu_0 \mathbf{curl} \underline{\mathbf{J}}_{\text{ext}} \text{ in } \mathbb{R}^3. \quad (12b)$$

152 Note that, if one chooses  $\underline{\mathbf{J}}_{\text{ext}}$  so that  $\text{div}(\underline{\mathbf{J}}_{\text{ext}}) = 0$ , then  $(\underline{\mathbf{E}}, \underline{\mathbf{H}}) \in \mathbf{H}_{\text{loc}}(\mathbf{curl})^2$  solution of (12) or  
 153 (11) also belongs to  $\mathbf{V}_{\text{loc}}(\hat{\varepsilon}; \mathbf{curl}) \times \mathbf{V}_{\text{loc}}(\mu_0; \mathbf{curl})$ , with  $\mathbf{V}_{\text{loc}}(\zeta; \mathbf{curl}) := \{\mathbf{X} \in \mathbf{H}_{\text{loc}}(\mathbf{curl}) \mid \text{div}(\zeta \mathbf{X}) =$   
 154  $0\}$ .

155 Contrary to the time-domain case, due to the change of sign of  $\hat{\varepsilon}_r$  at optical frequencies,  
 156 the problems (11)-(12) can be ill-posed in  $\mathbf{V}_{\text{loc}}(\hat{\varepsilon}; \mathbf{curl}) \times \mathbf{V}_{\text{loc}}(\mu_0; \mathbf{curl})$ . With the T-coercivity  
 157 approach it has been shown (e.g. [25, 16, 26, 17, 18, 20, 21]) that there exists two cases depending  
 158 on the contrast  $\kappa_\varepsilon := \frac{\varepsilon_m}{\varepsilon_d}$ :

159 • for contrasts  $\kappa_\varepsilon$  far enough from  $-1$ , then the problem is well-posed in  $\mathbf{V}_{\text{loc}}(\hat{\varepsilon}; \mathbf{curl}) \times$   
 160  $\mathbf{V}_{\text{loc}}(\mu_0; \mathbf{curl})$ .

161 • for contrasts  $\kappa_\varepsilon$  close to  $-1$ , plasmonic hypersingularities arise at the corners of the inter-  
 162 face (if any), and the problems is ill-posed in  $\mathbf{V}_{\text{loc}}(\hat{\varepsilon}; \mathbf{curl}) \times \mathbf{V}_{\text{loc}}(\mu_0; \mathbf{curl})$ .

163 Those guidelines can be refined for the specific case of Maxwell 2D. In that case the interval  
 164 of contrasts (acceptable or not) is explicitly known. For now, let us denote  $I_c$  this interval. We  
 165 will provide explicit bounds if needed for numerical purposes. Let us note that this interval  $I_c$   
 166 corresponds to a *critical interval* of angular frequencies  $I_\omega$ , and that it holds that

$$\kappa_\varepsilon = -1 \quad \text{if, and only if,} \quad \omega := \omega_{sp} := \frac{\omega_p}{\sqrt{\varepsilon_d + \varepsilon_\infty}} \quad (13)$$

167 with  $\omega_{sp}$  denoting the surface plasmon angular frequency. The specific case  $\omega = \omega_{sp}$  is very  
 168 peculiar and the problem is strongly-ill posed. In what follows we will exclude this case.

169 To sum up, in the frequency-domain, there is a critical range of angular frequencies for which  
 170 the problem is then ill-posed, whereas in the time-domain the problem is always mathematically  
 171 well-posed. This interesting result questions the validity of the limiting amplitude principle at  
 172 critical angular frequencies, indicating that

- 173 • If  $\omega \notin I_\omega$ : the limiting amplitude principle holds.
- 174 • If  $\omega \in I_\omega$ : the limiting amplitude should not hold.

175 Using this conjecture, the rest of the paper is dedicated to provide several approaches and results  
 176 to find signature of the critical interval  $I_\omega$  in time-domain simulations. To that aim we will need  
 177 to compute quantities of interest in frequency-domain.

178 **Remark 5.** *The limiting amplitude principle has been studied for Lorentz metamaterials (both*  
 179 *permeability and permittivity can change sign in frequency-domain) for planar interfaces. It has*  
 180 *been shown that this principle doesn't hold for  $\kappa_\varepsilon = -1$ , and that in this case the fields' amplitude*  
 181 *increases linearly with respect to time [15].*

182 *Electromagnetic energy, Poynting vector and Cross sections.* Time-domain quantities such as  
 183 the electromagnetic energy and the Poynting vector can be compared to frequency-domain ones  
 184 if harmonic behavior is achieved. In the time-domain, we consider a real-valued harmonic ex-  
 185 citation of the form  $\mathbf{J}_{e,xt}(\mathbf{x}, t) = \Re(\underline{\mathbf{J}}_{e,xt}(\mathbf{x})e^{-i\omega t})$ , with  $\omega > 0$  and  $\underline{\mathbf{J}}_{e,xt}$  a complex-valued field.  
 186 If we denote  $(\underline{\mathbf{E}}, \underline{\mathbf{H}})$  the solution of (9) with source term  $\underline{\mathbf{J}}_{e,xt}$ , then if the solution of (4) is har-  
 187 monic, it should write as  $(\mathbf{E}(\mathbf{x}, t), \mathbf{H}(\mathbf{x}, t), \mathbf{J}(\mathbf{x}, t)) = \Re(\underline{\mathbf{E}}(\mathbf{x})e^{-i\omega t}, \underline{\mathbf{H}}(\mathbf{x})e^{-i\omega t}, \underline{\mathbf{J}}(\mathbf{x})e^{-i\omega t})$ . Then to  
 188 relate frequency- and time-domain energy, the adequate quantity to start with is the time average  
 189 energy

$$\underline{\mathcal{E}} = \frac{1}{T(\omega)} \int_{t_0}^{t_0+T(\omega)} \mathcal{E}(t) dt, \quad (14)$$

190 where  $T(\omega)$  is equal to the time period, i.e.  $T(\omega) = 2\pi\omega^{-1}$ , and  $t_0 \geq 0$ . Using expression (6), the  
 191 average energy becomes<sup>4</sup>

$$\begin{aligned} \underline{\mathcal{E}} &= \frac{1}{2T(\omega)} \int_{t_0}^{t_0+T(\omega)} \left\| \frac{\sqrt{\varepsilon}}{2} (\underline{\mathbf{E}}e^{-i\omega t} + \underline{\mathbf{E}}^*e^{i\omega t}) \right\|_{L^2(\mathbb{R}^3)}^2 + \left\| \frac{\sqrt{\mu_0}}{2} (\underline{\mathbf{H}}e^{-i\omega t} + \underline{\mathbf{H}}^*e^{i\omega t}) \right\|_{L^2(\mathbb{R}^3)}^2 \\ &\quad + \frac{1}{\varepsilon_0\omega_p^2} \left\| \frac{1}{2} (\underline{\mathbf{J}}e^{-i\omega t} + \underline{\mathbf{J}}^*e^{i\omega t}) \right\|_{L^2(\mathbb{R}^3)}^2 dt, \quad (15) \\ &= \frac{1}{4} \left( \left\| \sqrt{\varepsilon} \underline{\mathbf{E}} \right\|_{L^2(\mathbb{R}^3)}^2 + \left\| \sqrt{\mu_0} \underline{\mathbf{H}} \right\|_{L^2(\mathbb{R}^3)}^2 + \frac{1}{\varepsilon_0\omega_p^2} \left\| \underline{\mathbf{J}} \right\|_{L^2(\mathbb{R}^3)}^2 \right), \end{aligned}$$

192 with  $\underline{\mathbf{V}}^*$  denoting the complex conjugate of  $\underline{\mathbf{V}}$ .

193 **Remark 6.** *We here point out a very straightforward fact that will be used later in the computa-*  
 194 *tions. For the time-domain fields to have a harmonic behavior, the time average of the energy on*  
 195 *an interval of length  $T(\omega)$  must not depend on the chosen interval. This simple remark provides*  
 196 *us with a necessary condition for a signal to be harmonic.*

---

<sup>4</sup>Recall that  $\underline{\mathbf{J}} = 0$  in  $\mathbb{R}^3 \setminus \tilde{\Omega}$ .

197 Similarly, we can compute the time average Poynting vector over the time period  $T(\omega)$  defined  
 198 as follows:

$$\underline{\Pi}(\omega) = \frac{1}{T(\omega)} \int_{t_0}^{t_0+T(\omega)} \underline{\Pi}(t) dt = \frac{1}{2} \Re(\underline{\mathbf{E}} \times \underline{\mathbf{H}}^*). \quad (16)$$

199 We will omit to write the space dependence using the abuse of notations  $\underline{\Pi}(\omega) = \underline{\Pi}(\cdot, \omega)$ ,  
 200  $\underline{\Pi}(t) = \underline{\Pi}(\cdot, t)$ .

201 To further exploit information from the Poynting vector, it is natural to introduce physical  
 202 quantities called cross sections. As introduced in Remark 2, we separate the contributions from  
 203 the scattered fields  $(\underline{\mathbf{E}}_{sca}, \underline{\mathbf{H}}_{sca})$  and the incident fields  $(\underline{\mathbf{E}}_{inc}, \underline{\mathbf{H}}_{inc})$ : we define  $\underline{\Pi}_{sca} = \underline{\mathbf{E}}_{sca} \times \underline{\mathbf{H}}_{sca}$ ,

$$\underline{\Pi}_{sca}(\omega) = \frac{1}{T(\omega)} \int_{t_0}^{t_0+T(\omega)} \underline{\Pi}_{sca}(t) dt, \text{ and similarly } \underline{\Pi}_{inc} \text{ using the incident electromagnetic fields.}$$

205 Note that  $|\underline{\Pi}_{inc}|$  is independent of the spatial variables.

206 To quantify the amount of absorbed energy  $\underline{P}_{abs}$  and scattered energy  $\underline{P}_{sca}$  at a given pulsation,  
 207 we compute the fluxes of, respectively, the total Poynting vector  $\underline{\Pi}$  and the scattered Poynting  
 208 vector  $\underline{\Pi}_{sca}$  on a closed surface  $S$  enclosing the scatterer:

$$\underline{P}_{abs}(\omega) =: - \int_S \underline{\Pi}(\omega) \cdot \mathbf{n} dS, \quad \underline{P}_{sca}(\omega) =: - \int_S \underline{\Pi}_{sca}(\omega) \cdot \mathbf{n} dS, \quad (17)$$

209 where  $\mathbf{n}$  is the outward normal vector to  $S$ . If one denotes by  $V$  the bounded volume such that  
 210  $S = \partial V$ , one has obviously  $\underline{P}_{abs}(\omega) = - \int_V \text{div} \underline{\Pi}(\omega) d\mathbf{x}$ . If there is a scatterer in the domain,  
 211 not all the energy entering the volume delimited by  $S$  will leave it: some energy is absorbed  
 212 ( $\underline{P}_{abs}(\omega) > 0$ ). The cross sections are then defined relative to the power density (per unit area) of  
 213 the incident field:

$$C_{abs} = \frac{\underline{P}_{abs}}{|\underline{\Pi}_{inc}|}, \quad C_{sca} = \frac{\underline{P}_{sca}}{|\underline{\Pi}_{inc}|}, \quad (18)$$

214 where  $C_{abs}$  denotes the absorption cross section,  $C_{sca}$  the scattering cross section<sup>5</sup>. These frequency-  
 215 domain quantities are widely used to measure the absorption or the scattering features of a given  
 216 scatterer. For some standard structures, it is also possible to have their analytical expression (see  
 217 *e.g.* [27] and references therein).

### 218 3. The two-dimensional case: theoretical and numerical guidelines

219 We focus on the light scattering by a rod structure with transversal section  $\mathbb{D}$ . We seek  
 220 solutions of system (4) that have an invariance with respect to the direction of the rod's axis.  
 221 In this setting the tridimensional Maxwell's equations can be recast in two 2D sets of equations  
 222 defining two transverse modes: TE (Transverse Electric) and TM (Transverse Magnetic).

223 In the rest of this paper, we consider that  $\Omega$  is a metallic rod of bounded section  $\mathbb{D}$ ,  $\Omega := \mathbb{D} \times \mathbb{R}$   
 224 and we concentrate on the 2D TM polarization. Then  $(\vec{E}_\perp, H_z, \vec{J}_\perp)$ , with  $\vec{V}_\perp := (V_x, V_y)^t$ , is  
 225 solution of the corresponding two-dimensional version of Maxwell's equations.

<sup>5</sup>one can also define  $C_{ext}$ , the extinction cross section as  $C_{ext} = C_{abs} + C_{sca}$ . It will not be used in this work.

226 *3.1. An explicit theoretical critical interval*

227 As mentioned previously, there exists a critical interval  $I_\omega$ , centered around the surface plas-  
 228 mon frequency  $\omega_{sp}$ , for which the problem is ill-posed in frequency-domain. In some cases, this  
 229 interval is explicitly known, and hypersingular behaviors have been identified in the ill-posed  
 230 configurations. We will use this framework to assert if the limiting amplitude principle holds.

231 According to (11a), in frequency-domain, the problem in  $\underline{H}_z$  becomes

$$\operatorname{curl} \hat{\varepsilon}_r^{-1} \operatorname{curl} \underline{H}_z - k^2 \underline{H}_z = -\operatorname{curl} \hat{\varepsilon}_r^{-1} \vec{J}_{ext,\perp} \text{ in } \mathbb{R}^2,$$

232 and similarly for the problem in  $\underline{E}_\perp$  (cf. (12b)). Classical theory considers  $\vec{E}_\perp \in \mathbf{L}_{loc}^2(\mathbb{R}^2)$  so that  
 233  $\underline{H}_z \in H_{loc}^1(\mathbb{R}^2)$ , and the bounds of the interval  $I_c$  depends on the interface's geometry. Suppose  
 234 that the interface  $\Sigma := \partial\mathbb{D}$  is polygonal with  $0 < \alpha < 2\pi$  the sharpest interior angle in  $\mathbb{D}$ . We  
 235 define  $I_\alpha := \max\left(\frac{\alpha}{2\pi-\alpha}; \frac{2\pi-\alpha}{\alpha}\right) > 1$ , then  $I_c := [-I_\alpha; -1/I_\alpha]$  (details about the derivation can be  
 236 found in [16, Theorem 3.3], [28, Theorem 1]). This gives us

$$\begin{aligned} -I_\alpha \leq \kappa_\varepsilon \leq -\frac{1}{I_\alpha} &\iff \frac{\omega_p}{\sqrt{I_\alpha \varepsilon_d + \varepsilon_\infty}} \leq \omega \leq \frac{\omega_p}{\sqrt{\varepsilon_\infty + \frac{\varepsilon_d}{I_\alpha}}}, \\ I_\omega &:= \left[ \frac{\omega_p}{\sqrt{I_\alpha \varepsilon_d + \varepsilon_\infty}}; \frac{\omega_p}{\sqrt{\varepsilon_\infty + \frac{\varepsilon_d}{I_\alpha}}} \right] \end{aligned} \quad (19)$$

237 Moreover, we have the following result:

- 238 • If  $\omega \notin \left[ \frac{\omega_p}{\sqrt{I_\alpha \varepsilon_d + \varepsilon_\infty}}; \frac{\omega_p}{\sqrt{\varepsilon_\infty + \frac{\varepsilon_d}{I_\alpha}}} \right]$ : problem in  $\underline{H}_z$  is well-posed in  $H_{loc}^1(\mathbb{R}^2)$ . Mathematical  
 239 well-posedness in this function space guarantees to have a bounded total electromagnetic  
 240 energy.
- 241 • If  $\omega \in I_\omega \setminus \{\omega_{sp}\}$ : problem in  $\underline{H}_z$  is ill-posed in  $H_{loc}^1(\mathbb{R}^2)$ . There exist black-hole waves  
 242  $s \notin H_{loc}^1(\mathbb{R}^2)$  that propagate towards the corners.

243 **Remark 7.** Given a polygonal interface  $\Sigma$  with  $N$  corners  $c_i$ ,  $i = 1, \dots, N$ , and denoting  $\alpha_i$ ,  
 244  $i = 1, \dots, N$  all the interior angles in  $\mathbb{D}$ , one can define subintervals

$$I_{c_i} := [-I_{\alpha_i}; -1/I_{\alpha_i}], \text{ and } I_{c_i} \subseteq I_c, i = 1, \dots, N, \text{ or equivalently } I_{\omega_i} \subseteq I_\omega, i = 1, \dots, N.$$

245 This means that, depending on the contrast  $\kappa_\varepsilon$  (and therefore depending on the angular frequency  
 246  $\omega$ ), all black-hole waves, or only some of them, can be excited. This will play a certain role when  
 247 interpreting numerical results.

248 **Remark 8.** Black-hole waves can be characterized as follows. Given a corner  $c$ , we denote  
 249  $(r, \theta)$  the polar coordinates centered at  $c$ , the black-hole wave propagating towards the corner  $c$   
 250 is of the form  $s(r, \theta) = r^{i\lambda} \Phi(\theta)$ , with  $\lambda \in \mathbb{R}^*$ , and  $\Phi$  a periodic function. Moreover it has been  
 251 established that (see [20] for details):

- 252 • If  $\omega \in \left[ \frac{\omega_p}{\sqrt{I_\alpha \varepsilon_d + \varepsilon_\infty}}, \omega_{sp} \right)$ , the black-hole wave is an odd coupled plasmon. This means  
 253 that the black-hole wave exhibits two localized oscillating behaviors along the interface  
 254 that are skew-symmetric with respect to the angle's bisector ( $\Phi$  is an odd function).

- 255 • If  $\omega \in \left( \omega_{sp}, \frac{\omega_p}{\sqrt{\varepsilon_\infty + \frac{\varepsilon_d}{I_\omega}}} \right]$ , the black-hole wave is an even coupled plasmon. This means that  
 256 the black-hole wave exhibits two localized oscillating behaviors along the interface that  
 257 are symmetric with respect to the angle's bisector ( $\Phi$  is an even function).

258 Figure 1 represents the two types of black-hole waves near a corner.

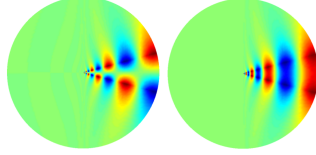


Figure 1: Representation of black-hole waves near a corner: odd (left), and even (right).

259 **Remark 9.** The specific case  $\omega = \omega_{sp}$  is strongly ill-posed, the provided black-hole characteri-  
 260 zation is valid for  $\omega \in I_\omega \setminus \{\omega_{sp}\}$ . We refer for example to [15, 19, 29] for more details.

261 The two-dimensional case is fully characterized in frequency-domain. It provides the ade-  
 262 quate framework to investigate if the limiting amplitude principle holds in plasmonic structures.  
 263 In particular, we will look for a signature of this critical interval  $I_\omega$  in time-domain.

### 264 3.2. Physical problem

265 In order to investigate situations with corners, we choose an isosceles triangle of upper aper-  
 266 ture  $\frac{\pi}{6}$ , with characteristic size (height of longest bisector) equal to 20nm for the transversal  
 267 section  $\mathbb{D}$  (see Figure 2) and with area  $a_T \approx 1.07 \times 10^{-16} \text{m}^2$ . It is tilted so that the edge  $ab$  is  
 268 vertical.

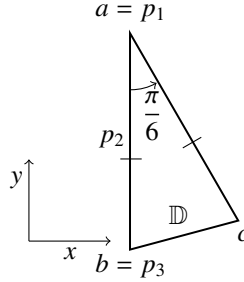


Figure 2: Physical domain and notations. 2D section in the  $(x, y)$ -plane of the metallic rod.

269 The exterior domain  $\mathbb{R}^2 \setminus \bar{\mathbb{D}}$  is filled with vacuum ( $\varepsilon_d = 1$ ). The section  $\mathbb{D}$  will either consist  
 270 of

- 271 (i) Dielectric:  $\varepsilon_\infty = 3.73$ ,  $\omega_p = 0 \text{rad.s}^{-1}$ .  
 272 (ii) Gold:  $\varepsilon_\infty = 1$ ,  $\omega_p = 13.87 \times 10^{15} \text{rad.s}^{-1}$ , with values taken from [30].  
 273 (iii) Another Drude material:  $\varepsilon_\infty = 3.7362$ ,  $\omega_p = 13.87 \times 10^{15} \text{rad.s}^{-1}$ .

274 We will illuminate the structure at a range of pulsations  $[\omega_{min}, \omega_{max}]$  that includes the critical  
 275 interval  $I_\omega$  associated to both materials<sup>6</sup> and that is such that  $\omega_{max} \leq \omega_p$ . Therefore the smallest  
 276 wavelength is greater than  $\frac{2\pi c_0}{\omega_p} \approx 135\text{nm}$ , with  $c_0 = \frac{1}{\sqrt{\epsilon_0 \epsilon_d \mu_0}}$ . In this regard, the metallic structure  
 277 is subwavelength for incident illuminations below the plasma angular frequency  $\omega_p$ .

278 Some quantities will be visualized at three selected probe points:  $p_1$  situated at the top vertex  
 279  $a$ ,  $p_2$  is the middle of segment  $[ab]$  and  $p_3$  situated at the left bottom vertex  $b$ . To investigate the  
 280 limiting amplitude principle, we use an incident illumination  $(\vec{E}_{\perp,inc}, \vec{H}_{z,inc})$  (added to radiation  
 281 conditions). The latter will be

- 282 (a) a monochromatic plane wave (solution of Maxwell's in vacuum), or
- 283 (b) a polychromatic gaussian pulse (Gaussian modulated plane wave).

284 We choose the vertical direction of propagation  $-y$  for the incident plane wave field. By tilting  
 285 the triangle, we break the symmetry, allowing us to excite both odd and even coupled plasmons.

### 286 3.3. Limiting amplitude principle requirements

287 The monochromatic case (a) is readily covered by the limiting amplitude principle frame-  
 288 work. Indeed, as already mentioned in Remark 2, the total electromagnetic field can then be  
 289 decomposed into the incident contribution  $(\vec{E}_{inc,\perp}, \vec{H}_{inc,z})$  and the scattered one  $(\vec{E}_{sca,\perp}, \vec{H}_{sca,z})$ .  
 290 As a result, the scattered field  $(\vec{E}_{sca,\perp}, \vec{H}_{sca,z})$  verifies Maxwell's equations with homogeneous  
 291 radiation conditions and source term  $\vec{J}_{ext,\perp}$  with support in  $\mathbb{D}$ . This source term expresses the fact  
 292 that the incident plane wave  $(\vec{E}_{inc,\perp}, \vec{H}_{inc,z})$  is solution of Maxwell's equation in vacuum, but is  
 293 not solution in the scatterer. Since the incident field is monochromatic, so is the source term. In  
 294 other words, our source term is monochromatic, with support  $\subseteq \mathbb{R}^2$  and in  $L^2(\mathbb{R}^2)$  which fits in  
 295 the theoretical framework led by [11, 12] to investigate the limiting amplitude principle.

296 Same procedure can be applied with the Gaussian modulated plane wave (b). However, in  
 297 this case, the resulting source term  $\vec{J}_{ext,\perp}$  in the scattered field equation is not monochromatic  
 298 anymore. The latter is in addition attenuated. This case does not readily fall into the limiting  
 299 amplitude principle framework. However, such an incident field allows for the excitation of the  
 300 scatterer by a whole range of pulsations using one single excitation. Moreover, using Fourier  
 301 transform, the spectral response of the scatterer is easily attainable once the time-domain fields  
 302 are known. Source (b) provides a practical (but empirical) approach to investigate the problem.

### 303 3.4. Numerical framework and strategy

304 In what follows, we will need to compute a numerical approximation of the solution of the  
 305 time-domain equations. To do so, we consider a Discontinuous Galerkin Time Domain (DGTD)  
 306 framework as developed in [31]. This numerical framework is particularly adapted to the chal-  
 307 lenges encountered for scattering problems and has been assessed on several occasions especially  
 308 for plasmonic problems (see *e.g.* [32, 33] and references therein). In the numerical tests, we use  
 309 a non-dissipative DGTD scheme for the whole system with unknowns  $(\mathbf{E}, \mathbf{H}, \mathbf{J})$ . It relies on a  
 310 discontinuous Galerkin finite element space discretization (with Lagrange nodal basis) with centered  
 311 fluxes, and a leap-frog scheme in time. This scheme has the advantage to be explicit; the

---

<sup>6</sup>Here, if  $\tilde{\omega} \in I_\omega$ , then  $\tilde{\omega} \leq \frac{\omega_p}{\sqrt{\epsilon_{\infty} + \frac{\epsilon_d}{\epsilon_a}}} \leq \omega_p$ .

312 price to pay is that one should choose discretization parameters according to a CFL constraint.  
 313 Computations are made on an adimensionalized version of the system, quantities plotted later in  
 314 the paper have been re-dimensionalized.

315 We approximate the solution over a sufficiently long physical time  $T$  relative to the period  
 316 of the incident signal:  $T$  represents 100 to 200 times the period of the monochromatic source  
 317 (a), or the period of the smallest frequency in the pulse of the polychromatic source (b). This  
 318 time has been empirically adjusted so that it does not affect our conclusions with regards to the  
 319 convergence of the computed quantities. We are able to compute all the quantities mentioned  
 320 in Section 2: time evolution of the energy, time evolution of the fields at probe points, and time  
 321 averaged quantities. In particular, we compute the discrete time evolution of the total discrete  
 322 energy (on the whole computational domain) and in a small domain surrounding each corner.  
 323 When considering a polychromatic source (b), we compute cross sections and Poynting fluxes at  
 324 the end of the simulation, using a Fourier transform that is computed "on the fly" (done in one  
 325 simulation run). For illuminations considered in this work, the quantity  $|\underline{\Pi}_{inc}|$  that appears in (18)  
 can be computed analytically.

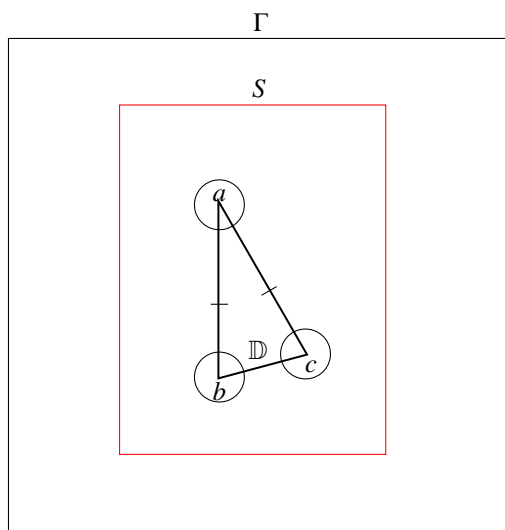


Figure 3: The computational domain is delimited by an artificial boundary  $\Gamma$ . A side of  $\Gamma$  has a length of 60nm. The cross sections are computed on a line  $S$  around the scatterer, which is approximately 20nm away from it. The black-hole fluxes and energy are computed in small disks centered at each corner.

326 As mentioned previously, the monochromatic source type (a) falls into the exact limiting  
 327 amplitude principle setting, and therefore will be used to find a clear indication of a non-harmonic  
 328 response to the harmonic incident field. The polychromatic source type (b) will allow to obtain  
 329 a spectral response and investigate physical quantities over the whole spectral band of interest,  
 330 and in one single run. The two approaches are thus complementary and are used to thoroughly  
 331 test our approach.

333 The scheme has been implemented in a in house 2D Fortran code developed within the Inria  
 334 Atlantis project team (Inria Sophia Antipolis, France)<sup>7</sup>. Previous versions of this code have

<sup>7</sup><http://www-sop.inria.fr/atlantiss/>

335 been already exploited in the context of [34] and [35]. Discretization parameters have been  
 336 fixed so that we use a discretization fine enough with respect to the incident wavelength and  
 337 fulfill the CFL condition. If  $\Delta t$  denotes the physical time step, and  $h_{max}$  the space discretization  
 338 parameter, we use  $\Delta t \approx 10^{-19}$ s and  $h_{max} \approx 1$ nm (the mesh is non uniform and is appropriately  
 339 refined at the corners of the domain and close to the interface, where the size of the mesh is  
 340 approximately  $\frac{1}{5}h_{max}$ ). Unless specified, we use a  $\mathbb{P}_2$  (polynomials of degree less than or equal to  
 341 2) basis for our finite element space. Finally, in Figure 3 we detail the *computational domain* and  
 342 geometrical entities that we use to compute the solution and quantities of interest. Numerically,  
 343 one computes Poynting fluxes, called *black-hole fluxes* for short, around each corner, for  $\omega$  in the  
 344 range of pulsations of interest:

$$F_k(\omega) := \int_{D_k} \operatorname{div} \underline{\Pi}(\omega) d\mathbf{x}, \quad k = \{a, b, c\}, \quad (20)$$

345 where  $(D_k)_{k=\{a,b,c\}}$  are (small) disks of radius 2nm around each corner  $a, b, c$ , respectively. Simi-  
 346 larly, the energies at the vicinity of each corner are computed for  $k = \{a, b, c\}$  and  $t \in [0, T]$  using

$$\mathcal{E}_k(t) = \frac{1}{2} \|\sqrt{\varepsilon_0 \varepsilon_r} \vec{E}_\perp(t)\|_{L^2(D_k)}^2 + \frac{1}{2} \|\sqrt{\mu_0} H_z(t)\|_{L^2(D_k)}^2 + \frac{1}{2\varepsilon_0 \omega_p^2} \|\vec{J}_\perp(t)\|_{L^2(D_k)}^2. \quad (21)$$

#### 349 4. Numerical results

350 First, we investigate the situation where the limiting amplitude principle (LAP) holds. This  
 351 is the situation where one considers for example a dielectric inclusion (case (i) in Section 3.2).  
 352 We use this simple case as a benchmark to validate our strategy. Then, we consider situations  
 353 where the LAP might not hold (cases (ii) and (iii) in Section 3.2).

##### 354 4.1. When the limiting amplitude principle holds

355 We consider here case (i), of a dielectric inclusion<sup>8</sup>.

###### 356 4.1.1. Response to monochromatic illumination.

357 We consider a monochromatic incident field (a) of pulsation  $\omega$ , with  $\omega \in [2 \times 10^{15}, 13.8 \times 10^{15}]$   
 358 rad.s<sup>-1</sup>.

359 *Study of the energy.* Figure 4 represents the evolution of the electromagnetic energy  $\mathcal{E}$  over the  
 360 last 10% of the total physical time i.e.  $t \in [0.9T, T]$ , for some incident pulsations  $\omega$ . Results  
 361 show that the electromagnetic energy stays clearly bounded over time and is periodic. Moreover,  
 362 for each pulsation, we observe that the value of the energy mean  $\underline{\mathcal{E}}$  (see Figure 5) varies in the  
 363 range  $[2.255 \times 10^{-15}, 2.285 \times 10^{-15}]$ . Thus, it stays of the same order of magnitude over pulsations  
 364 and varies fairly little (relative variation of  $\approx 1\%$ ).

365 In the spirit of Remark 6, at each fixed pulsation  $\omega$ , we compute the mean value of the energy  
 366 over several time intervals of length  $T(\omega)$  (these intervals are chosen around the end of the  
 367 physical simulation time). We observe only relative variations of maximum  $10^{-6}$ , that allows us  
 368 to conclude that (for a fixed pulsation) the mean value of the energy is numerically independent  
 369 of the chosen interval: the signal appears to be harmonic at the expected frequency.

<sup>8</sup>To be complete, and for a further validation of the benchmark, the very simple case of vacuum has also been tested. The results are conclusive and as expected. We choose not to reproduce them here, since the situation is completely straightforward. The results will be only used sometimes for comparison, to support our reasoning.

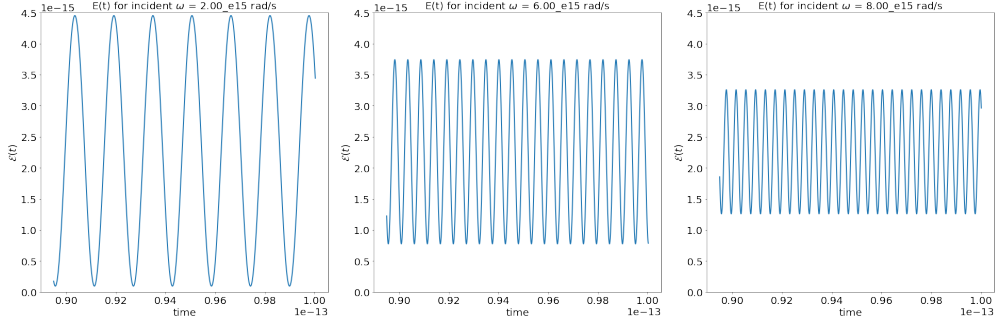


Figure 4: Representation of  $\mathcal{E}(t)$  (computed via (6)) for different incident fields. The incident field is monochromatic, we vary the pulsation  $\omega$  and represent the result for  $\omega = 2 \times 10^{15} \text{rad.s}^{-1}$ ,  $\omega = 6 \times 10^{15} \text{rad.s}^{-1}$ ,  $\omega = 8 \times 10^{15} \text{rad.s}^{-1}$ .

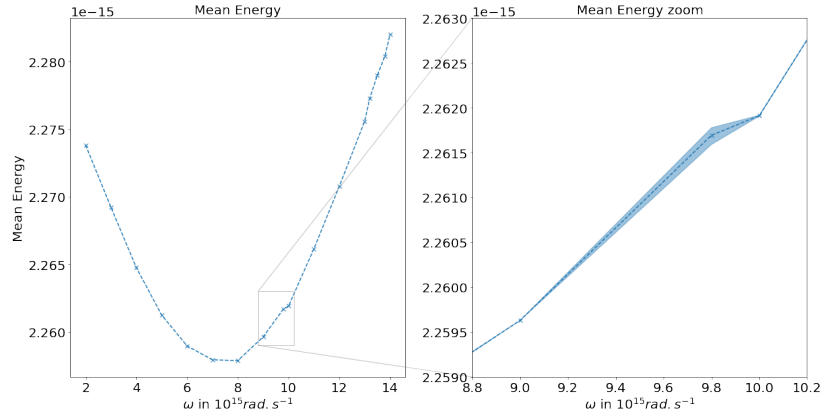


Figure 5: (Left) Mean energy  $\bar{\mathcal{E}}$  (computed with (15)) with respect to the incident pulsation. For each value of the pulsation  $\omega$ , we compute the mean of the energy on different time intervals of length  $T(\omega)$  over the simulation time duration. (Right) Zoom of the energy mean where there is a maximum of variations, scaled by a factor 10. Computations show relative variations of order  $10^{-6}$ .

370 *Fourier transform.* We now compute the Fourier transform (via FFT) of the magnetic field over  
 371 the range of frequencies of interest at chosen probe points (see Section 3.2), and compute the  
 372 relative error between the computed main pulsation and the chosen incident pulsation  $\omega$ . Figure  
 373 6 (Left) and Table 1 show that we recover harmonic signals centered within less than 0.4%  
 374 of relative error from the incident pulsation. To observe whether these effects are also visible  
 375 globally, we also plot in Figure 6 (right) the  $L^2$ -norm in space of the Fourier transform (in time)  
 376 of the total electromagnetic field. Here again, we recover a (numerical) harmonic behavior.  
 377 The above observations can be viewed as strong numerical evidences that the limiting amplitude  
 378 principle holds, as expected for dielectric materials.

#### 379 4.1.2. Response to polychromatic illumination

380 We also investigate the FFT of the magnetic field for a polychromatic illumination. We  
 381 choose here to represent the field  $H_z$  since this is the field that naturally compares to frequency-  
 382 domain approach via equation (11a), but we could have also represented the two components of

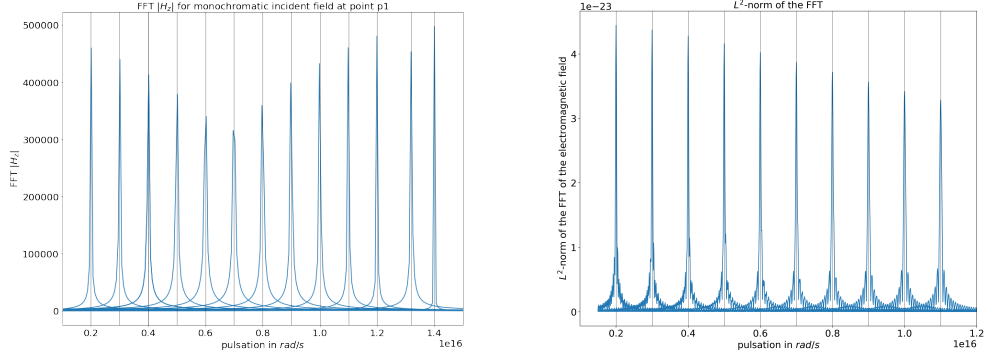


Figure 6: Left: FFT of  $H_z$  at first probe points  $p_1$ . Similar plots are obtained at other probe points and we do not represent them here to ease the reading. Right:  $L^2$ -norm of the FFT of the total electromagnetic field on the whole computational domain. Vertical lines represent the chosen incident  $\omega$ . All obtained peaks match the incident pulsation.

$\omega$ (rad.s $^{-1}$ )	Error $p_1$	Error $p_2$	Error $p_3$
2e15	4.61e-3	4.61e-3	4.61e-3
4e15	4.61e-3	4.61e-3	4.61e-3
6e15	4.61e-3	4.61e-3	4.61e-3
8e15	3.23e-3	3.23e-3	3.23e-3
10e15	1.66e-3	1.66e-3	1.66e-3
12e15	6.17e-4	6.17e-4	6.17e-4

Table 1: Relative errors of the computed main pulsations at the chosen probe points (via FFT) with the exact pulsation  $\omega$ , with  $\omega \in [2 \times 10^{15}, 12 \times 10^{15}] \text{rad.s}^{-1}$ .

383 the electric fields (leading to similar conclusions). This allows to: (i) alleviate any discrepancy in  
 384 the Fourier signal that may be sensitive to a single pulsation, (ii) test multiple incident pulsations  
 385 in one single run. Figure 7 represents the FFT of the magnetic field at probe points in the case  
 386 of propagation of a polychromatic pulse (b). Results show that a Gaussian Fourier signal is  
 387 recovered without any discrepancy. Same conclusion holds for the global  $L^2$ -norm of the Fourier  
 transform, that we do not reproduce here.

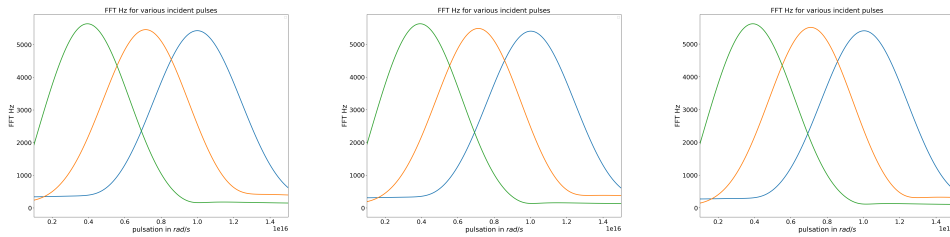


Figure 7: Modulus of the Fourier transform for various gaussian pulses at probe points  $p_1$  (left),  $p_2$  (middle),  $p_3$  (right) for several Gaussian pulses. We use several central frequencies ( $4 \times 10^{15}$ ,  $7 \times 10^{15}$  and  $10 \times 10^{15} \text{rad.s}^{-1}$ ).

389 *4.2. Breaking the limiting amplitude principle*

390 We now consider a metallic scatterer with parameters from case (ii) or (iii). We will follow  
391 the same strategy as in Section 4.1, but first we make use of results from Section 3.1.

392 *4.2.1. Explicit critical interval of pulsations*

393 In this section we specify  $I_\omega$  given in (19) for cases (ii) and (iii). Given the geometry, the  
394 critical interval is associated to corner  $a$  with aperture  $\frac{\pi}{6}$  (then  $I_\alpha = 11$ ). Using Remark 7 we  
395 compute the critical subintervals associated to the other corners  $b, c$  to identify when black-hole  
396 waves may appear.

- 397 • For material (ii) (corresponding to gold) we obtain

$$\omega \in I_\omega \iff \frac{\omega_p}{\sqrt{12}} \leq \omega \leq \frac{\omega_p}{\sqrt{\frac{12}{11}}}$$

398 leading to  $I_\omega = [4.0039 \times 10^{15}, 13.2795 \times 10^{15}] \text{rad.s}^{-1}$ , and the surface plasmon angular  
399 frequency (13) is equal to

$$\omega_{sp} := \frac{\omega_p}{\sqrt{2}} \simeq 9.8076 \times 10^{15} \text{ rad.s}^{-1}.$$

400 The other two corners  $b, c$  of angle  $\frac{5\pi}{12}$ , provide  $I_{\omega_b} = I_{\omega_c} = [6.3307 \times 10^{15}, 12.3409 \times$   
401  $10^{15}] \text{rad.s}^{-1}$ .

- 402 • For material (iii) we obtain

$$\omega \in I_\omega \iff \frac{\omega_p}{\sqrt{11 + 3.7362}} \leq \omega \leq \frac{\omega_p}{\sqrt{3.7362 + \frac{1}{11}}}$$

403 leading to  $I_\omega = [3.6131 \times 10^{15}, 7.0899 \times 10^{15}] \text{rad.s}^{-1}$ , and the surface plasmon angular  
404 frequency (13) is equal to

$$\omega_{sp} := \frac{\omega_p}{\sqrt{1 + 3.7362}} \simeq 6.3732 \times 10^{15} \text{ rad.s}^{-1}.$$

405 Further we obtain  $I_{\omega_b} = I_{\omega_c} = [5.0524 \times 10^{15}, 6.9355 \times 10^{15}] \text{rad.s}^{-1}$ .

406 **Remark 10.** *In what follows, we will indicate  $I_\omega$  in light red, and the subinterval  $I_{\omega_b}$  in dark red*  
407 *in the plots.*

408 *4.2.2. Response to monochromatic illumination*

409 We consider a monochromatic incident field of pulsation  $\omega$ , with  $\omega \in [2 \times 10^{15}, 13.8 \times$   
410  $10^{15}] \text{rad.s}^{-1}$ . The covered pulsation range includes the critical interval  $I_\omega$  associated to both  
411 materials. Contrary to the previous case we expect changes for  $\omega \in I_\omega$ .

412 *Study of the energy.* Figure 8 represents the evolution of the energy for several incident pulsation  
413 values for both cases. Contrary to the previous case, we observe a drastic change of behavior  
414 of the energy when the pulsation  $\omega$  of the monochromatic source belongs to  $I_\omega$ : the energy  
415 drastically increases by several orders of magnitude ( $10^{-13}$  compared to  $10^{-15}$ ), and doesn't  
416 exhibit a clear periodic behavior. This change is clearly visible when  $\omega$  "enters" the critical  
417 interval. Moreover, at lower pulsations, the energy exhibits a periodic behavior. When  $\omega$  "leaves"  
418 the critical interval, the energy drastically decreases. For case (ii) it is not clear that we recover  
419 a periodic signal at the chosen pulsation (located right outside of the critical interval), however  
for case (iii) the periodic behavior for  $\omega \notin I_\omega$  is more visible. Figure 9 represents the means of

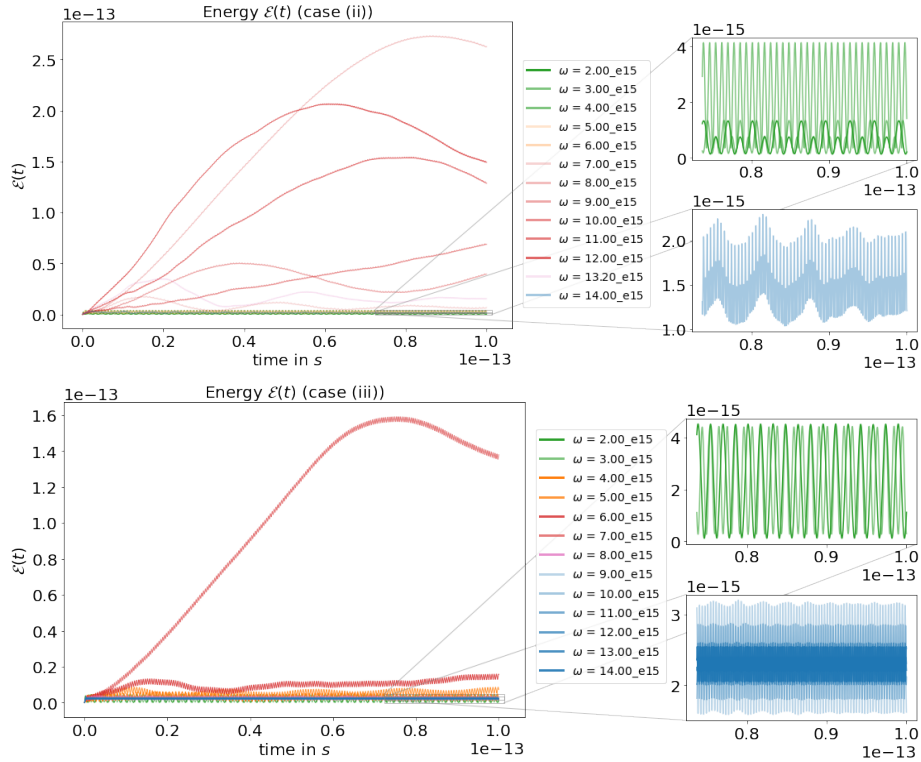


Figure 8: Representation of  $\mathcal{E}(t)$  (computed via (6)) for different incident fields for case (ii) (top) and for case (iii) (bottom), with zooms at the long time simulation. The green and blue curves correspond to  $\omega \notin I_\omega$ , whereas the warm colored curves correspond to  $\omega \in I_\omega$ .

420 energy  $\mathcal{E}$  with respect to the monochromatic pulsation. For each incident source, we compute the  
421 mean of the energy for different time intervals of length  $T(\omega)$  over the final part of the simulation  
422 time duration. The light blue shadow indicates the variations between those computations (we  
423 report the minimal and maximal values), scaled by a factor 10. As observed before, the energy  
424 is considerably more important at critical pulsations (indicated by the red zones). Additionally  
425 the computation of the mean  $\mathcal{E}$  is highly sensitive to the time interval when we choose  $\omega \in I_\omega$ ,  
426 indicating that a periodic regime may not be established. Note that the energy mean is two orders  
427 of magnitude stronger than what was observed in Section 4.1. Furthermore, one can observe that  
428 the strongest variations within the means are obtained when all corners are excited ( $\omega \in I_{\omega_b}$ ).  
429

430 Based on the energy observations, one can conclude that there is definitely a change of behavior  
 431 at critical pulsations, indicating that the limiting amplitude principle should not hold.

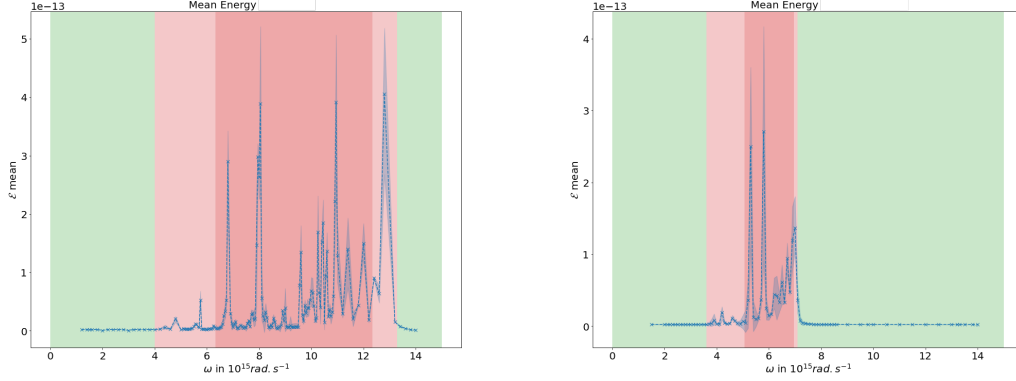


Figure 9: Mean of energy  $\underline{\mathcal{E}}$  (computed with (15)) with respect to the monochromatic pulsation: for case (ii) (left), for case (iii) (right). The green zones indicate when  $\omega \notin I_\omega$ , the red zones indicate when  $\omega \in I_\omega$ . The darker red zone indicates the critical subinterval  $\omega \in I_{\omega_b}$ .

431

432 *Fourier transform at probe points.* Figure 10 represents the Fourier transform of the magnetic  
 433 field over the range of frequencies of interest at probe point  $p_1$  (see Section 3.2). Similar plots  
 434 have been obtained for other probe points, we do not present them here. Figure 11 represents the  
 435  $L^2$ -norm in space of the Fourier transform (in time) of the whole electromagnetic field  $(\vec{E}_\perp, H_z)$ .

436 Results show that we still recover harmonic-like signals centered at the incident pulsation,  
 437 however the signal is perturbed for critical pulsations. We can make several observations:

- 438 • at each frequency, one main peak occurs at the pulsation of the incident field. The numer-  
 439 ical relative error to the exact value does not exceed the one obtained in Section 4.1,
- 440 • for some pulsations inside the critical interval, the main peak is wider and/or stronger in  
 441 intensity,
- 442 • for pulsations inside the critical subinterval, secondary peaks do appear.

443 The last two items above invalidate the limiting amplitude principle.

444 In the next section we compute the Fourier transform when considering a Gaussian pulse,  
 445 where the break of the harmonic signal is significantly more striking.

#### 446 4.2.3. Response to polychromatic illumination

447 We now investigate the response of the metallic scatterer to a pulse illumination (b). As  
 448 before, we investigate the Fourier transform of the magnetic field.

449 *Fourier transform.* Figure 12 represents the Fourier transform of the magnetic field at the probe  
 450 points  $p_1, p_2, p_3$  for a Gaussian pulse centered at  $4 \times 10^{15}, 7 \times 10^{15}$  and  $10 \times 10^{15}$   $\text{rad.s}^{-1}$ . One  
 451 clearly observes that the Gaussian signal is recovered for  $\omega \notin I_\omega$  and completely perturbed when  
 452  $\omega \in I_\omega$ . These effects are also observable globally. In Figure 13, we plot the  $L^2$ -norm (in space)  
 453 of the Fourier transform of the whole electromagnetic field  $(\vec{E}_\perp, H_z)$  (we here choose to represent  
 454 only one central frequency  $7 \times 10^{15}$   $\text{rad.s}^{-1}$ , the others being similar).

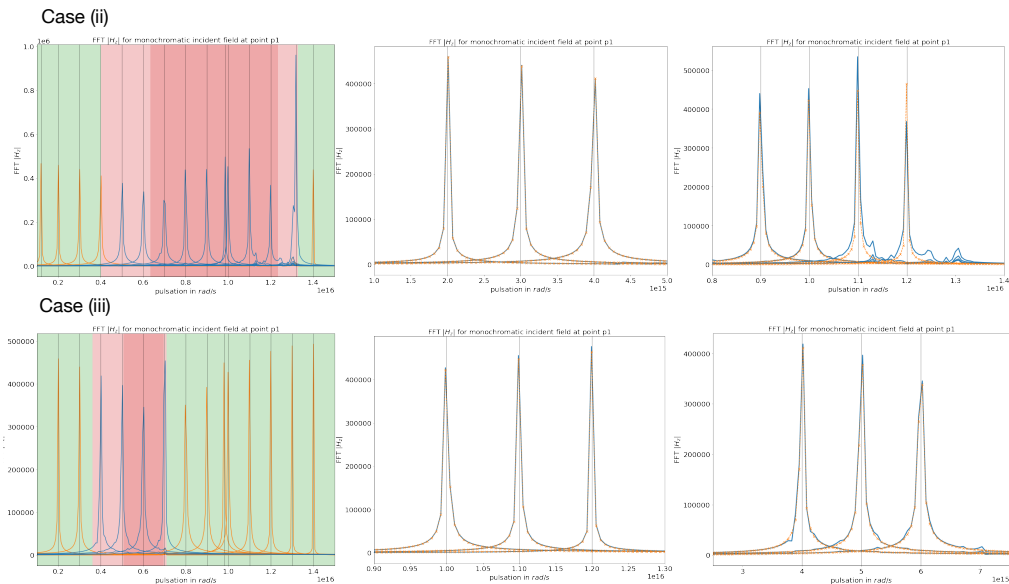


Figure 10: (Left) FFT of  $H_z$  at first probe point  $p_1$ : for case (ii) (top row), for case (iii) (bottom row). Vertical lines represent the chosen  $\omega$ . The green zones indicate when  $\omega \notin I_\omega$ , the red zones indicate when  $\omega \in I_\omega$ . The darker red zone indicates the critical subinterval  $\omega \in I_{\omega_b}$ . (Middle, Right): samples of FFT from the two cases: for  $\omega \notin I_\omega$  (middle), and for  $\omega \in I_\omega$  (right). The orange 'x' curves correspond to FFT peaks in vacuum (where the response is always harmonic).

#### 4.2.4. Conclusion

To sum up, through various quantities of interests, we can clearly identify a change of behavior in the spectral response in the critical interval. This provides numerical evidences about the proposed limiting amplitude principle conjecture. Moreover, using polychromatic pulse illumination, one is directly able to find precisely traces of the critical interval. In what follows, we continue our investigation and examine the impact of underlying black-hole waves on the time-domain simulations.

## 5. Black-hole waves resonances

Results from previous sections clearly highlight the break of the limiting amplitude principle for critical pulsations. In this section we investigate its impact on more physical quantities and situations.

### 5.1. Cross sections and black-hole fluxes

The amount of light diffracted or absorbed by an illuminated tridimensional structure is measured by energy fluxes. The intrinsic capacity of an object to diffract or absorb light is then measured relative to the power of the incident light beam excitation. One way to quantify this is to measure the diffraction or absorption cross sections (defined in (18)). As a matter of fact, these provide the equivalent area of the incident beam that would have to be used to obtain the same energy than that provided by the illuminated object. Thus when a scatterer absorbs or scatters light on a much larger area compared to its physical size, it transpires in the absorption and

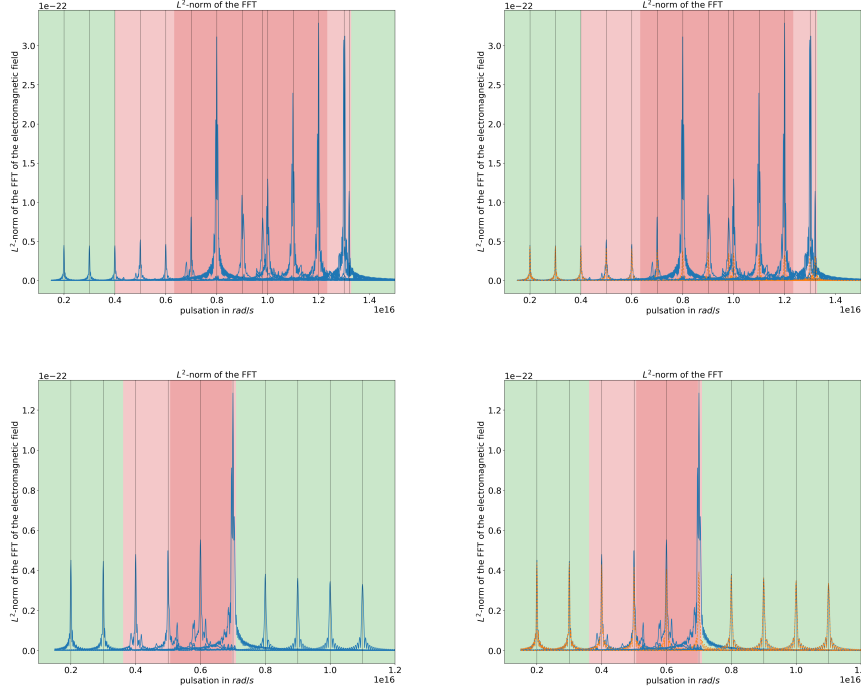


Figure 11:  $L^2$ -norm of FFT of the whole electromagnetic field (left) comparison with vacuum results (right): for case (ii) (top row), for case (iii) (bottom row). The orange ‘ $\times$ ’ curves correspond to FFT peaks in vacuum and the computations have been performed on same meshes for both cases. Vertical lines represent the chosen  $\omega$ . The green zones indicate when  $\omega \notin I_\omega$ , the red zones indicate when  $\omega \in I_\omega$ . The darker red zone indicates the critical subinterval  $\omega \in I_{\omega_b}$ .

474 scattering cross sections as intense peaks, and their location indicates the associated resonance  
 475 frequency. Cross sections are by nature positive and in the 2D setting that we consider, cross sec-  
 476 tions have the dimension of a length and provide an equivalent perimeter. We now investigate  
 477 how they vary for cases (ii) and (iii), in the context of a polychromatic illumination.

478 **Remark 11.** We choose a polychromatic source that illuminates the range of interest [ $1 \times$   
 479  $10^{15}$ ,  $14 \times 10^{15}$ ]  $rad.s^{-1}$ . With these chosen parameters, the range of frequencies at which we  
 480 illuminate the structure lies in the visible-near UV range. Furthermore, as mentioned in Section  
 481 3.2, the structure used is subwavelength.

482 *Cross sections.* Figure 14 represents the scattering and absorption cross sections obtained with  
 483 an incident Gaussian pulse for both Drude materials. It must be emphasized that our interest  
 484 lies more in finding a clear trace of the critical interval than in extracting a precise position of  
 485 resonances. Indeed, results show a clear trace of the critical interval: strong resonances do appear  
 486 for  $\omega \in I_\omega$ . While  $C_{sca}$  remains positive,  $C_{abs}$  presents quite significant unphysical oscillations  
 487 and negative values. We observe that the latter is also sensitive to mesh discretization and the  
 488 chosen degree of interpolation (even for a refined mesh).

489 These observations can be explained. Scattering cross section  $C_{sca}$  tracks the far-field’s re-  
 490 sponse whereas absorption cross section  $C_{abs}$  is linked to the near-field’s response of the scat-

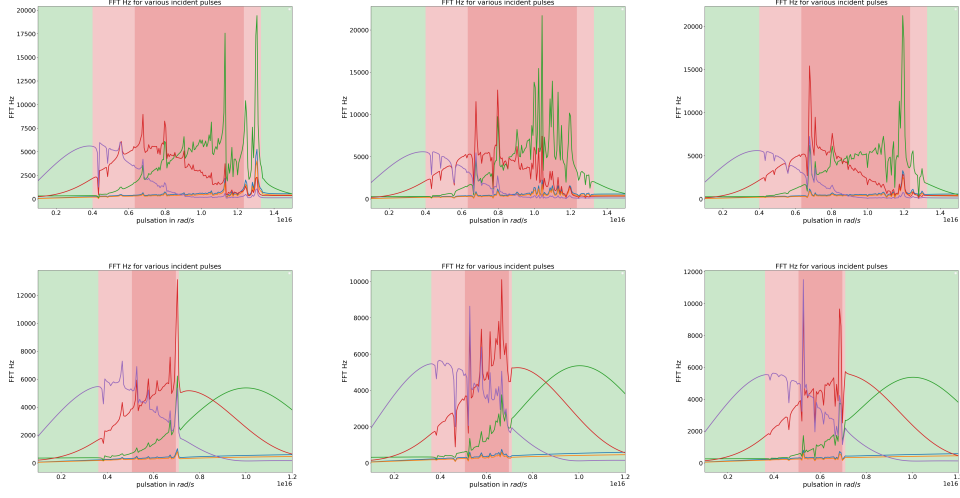


Figure 12: FFT of  $|H_z|$  at probe points  $p_1$  (left),  $p_2$  (middle),  $p_3$  (right) for several Gaussian pulses centered at  $4 \times 10^{15}$ ,  $7 \times 10^{15}$  or  $10 \times 10^{15}$   $\text{rad}\cdot\text{s}^{-1}$  and two widths: for case (ii) (top row), for case (iii) (bottom row). The green zones indicate when  $\omega \notin I_\omega$ , the red zones indicate when  $\omega \in I_\omega$ . The darker red zone indicates the critical subinterval  $\omega \in I_{\omega_b}$ .

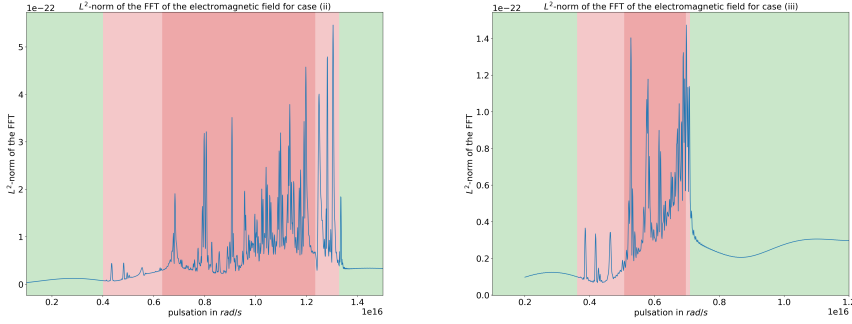


Figure 13:  $L^2$ -norm in space of the time FFT of the whole electromagnetic field for a Gaussian pulse centered at  $7 \times 10^{15}$   $\text{rad}\cdot\text{s}^{-1}$ : for case (ii) (left), for case (iii) (right). The green zones indicate when  $\omega \notin I_\omega$ , the red zones indicate when  $\omega \in I_\omega$ . The darker red zone indicates the critical subinterval  $\omega \in I_{\omega_b}$ .

491 terer. The more erratic behavior of  $C_{abs}$  can thus be explained by the difficulties to accurately  
 492 capture black-hole waves close to the corners, where discretization has to be fine enough to avoid  
 493 spurious reflections. This phenomenon has been well characterized in frequency-domain [20],  
 494 where an efficient modified finite element method (FEM) approximation with corner treatments  
 495 has been developed. Results may indicate that, even for time-domain formulations for which  
 496 the problem is mathematically well-posed, the discretization fails to approximate those highly-  
 497 oscillatory behaviors and would benefit from a similar specific corner treatment. This will be  
 498 part of future investigations. As mentioned before, while the polychromatic illumination doesn't  
 499 fit the theoretical LAP framework, it allows to highlight the predicted phenomena in a single

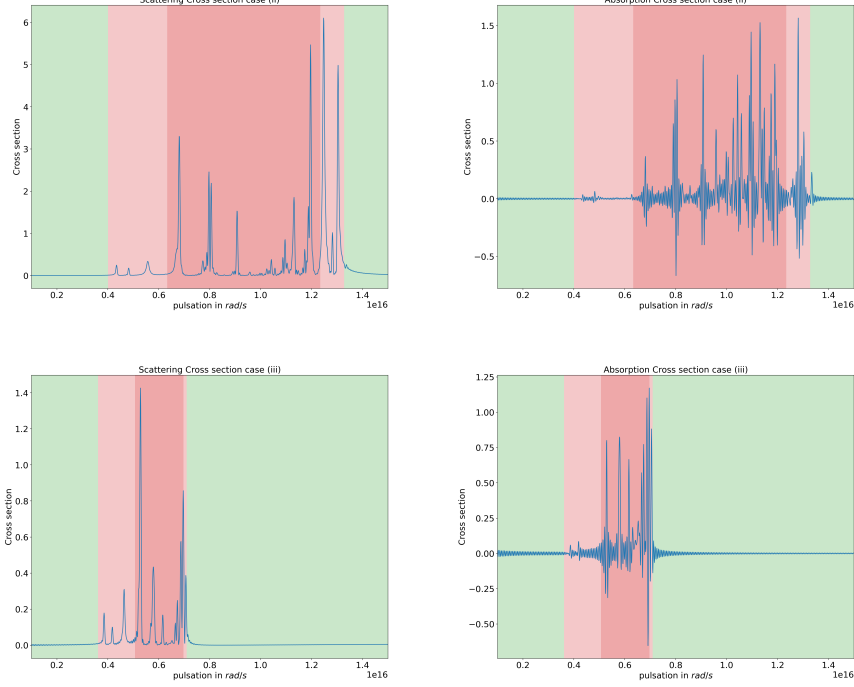


Figure 14: (Left): Scattering cross sections  $C_{sca}$  (computed with (18)) when considering a Gaussian pulse: for case (ii) (top row), for case (iii) (bottom row). (Right): Absorption cross sections  $C_{abs}$  when considering a Gaussian pulse: for case (ii) (top row), for case (iii) (bottom row).

500 run. This strongly suggests a systematic strategy to numerically identify signatures of a critical  
 501 interval on a given structure, even when the theory is not known.

502 *Poynting fluxes.* Figure 15 compares the total Poynting flux to the black-hole fluxes around each  
 503 corner of the triangle scatterer. The black-hole fluxes  $(F_k)_{k=\{a,b,c\}}$  are computed in a disk centred  
 504 at the corner and of radius 2nm, see (20) and Figure 3 for details. Results show that:

- 505 (i) all black-hole fluxes are (almost) equal to zero when  $\omega \notin I_\omega$  (no black-hole waves are  
 506 excited);
- 507 (ii) black-hole fluxes remain small when  $\omega \in I_\omega \setminus I_{\omega_b}$ , that is when only the black-hole singu-  
 508 larities located at the corner  $a$  can be excited;
- 509 (iii) all black-hole fluxes are significant when  $\omega \in I_{\omega_b}$  (corresponding to all black-hole singu-  
 510 larities being excited); in this situation, we also observe that almost all the contributions  
 511 to the Poynting flux are due to the corners.

512 All those observations are in accordance with theory from frequency-domain detailed in [20]:  
 513 this is closely related to black-hole excitation.

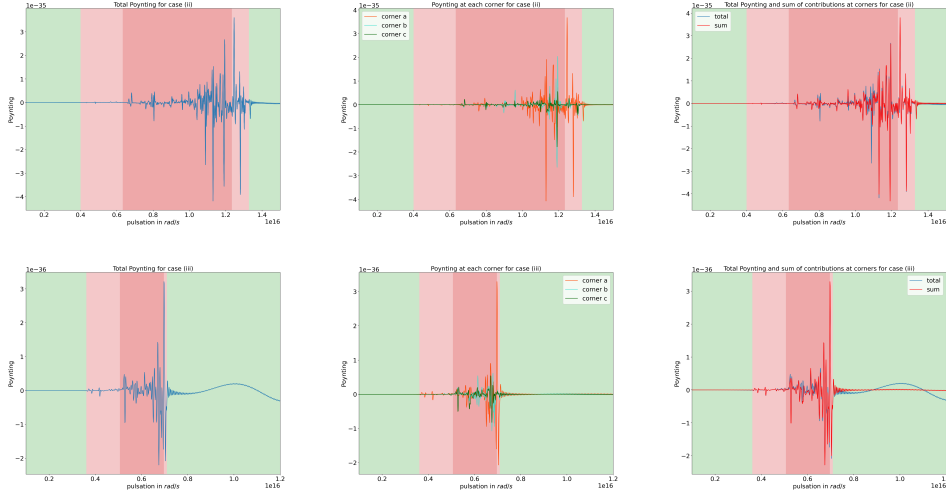


Figure 15: Poynting fluxes when considering a Gaussian pulse illumination, for case (ii) (top row) and for case (iii) (bottom row). We compute the total Poynting flux (left column), the black-hole fluxes (middle column), and compare the total Poynting flux to the sum of the black-hole fluxes (right column).

514 All results above illustrate that strong responses arise when illuminating a polyg-  
515 onal metallic obstacle with a source swiping critical pulsations  $\omega$ , and those strong behaviors are directly  
516 connected to the black-hole waves that are known to exist in frequency-domain. Here we con-  
517 sidered an *ideal* case without dissipation. In what follows we compare results with and without  
518 dissipation: this allows to identify whether the above observations are degenerate behaviors (i.e.  
519 they only occur in the absence of dissipation), or intrinsic behaviors (i.e. they are observable also  
520 with dissipation), of the physical structure.

## 521 5.2. Back to physics: the role of dissipation

522 Metals are always lossy, meaning that in practice one considers  $\gamma \neq 0$  in equation (4d). In  
523 this section we study the impact of introducing dissipation ( $\gamma \neq 0$ ) in our computations. Note  
524 that adding dissipation changes the asymptotics of the solution since the solution will be damped  
525 (up to vanishing). Moreover, problem (9) in frequency-domain is always mathematically well-  
526 posed in presence of dissipation. This implies that there are actually no critical pulsations to  
527 consider. We explore the question of finding a signature of the limit problem (and consequently  
528 limit behaviors) in lossy cases.

529 Figures 16 and 17 present comparisons between previous cross sections and Poynting fluxes,  
530 and the ones obtained when we add dissipation: we now consider models (ii) and (iii) with the  
531 physical value  $\gamma = 4.515 \times 10^{13} \text{rad.s}^{-1}$ . Obtained cross sections for lossy cases remain posi-  
532 tive (which is more physically relevant) and less sensitive to the mesh discretization. However  
533 in both configurations (non lossy, lossy), cross sections present similar behaviors: strong reso-  
534 nances arise at "critical" pulsations. Those resonances have less intensity with dissipation, and  
535 dissipation prevents strong spurious resonances mentioned above in the non lossy case (assuming  
536 the mesh is sufficiently refined at the corners). The fact that intense resonance peaks remain can

537 be explained via the frequency-domain framework [36, 20]. By adding dissipation, the frequency  
538 problem becomes well-posed, however strong oscillations at the corners remain. Dissipation al-  
539 lows to *attenuate the black-hole waves*,  $s \notin H_{\text{loc}}^1(\mathbb{R}^2)$  being replaced by  $s^\gamma \in H_{\text{loc}}^1(\mathbb{R}^2)$ , and selects  
540 the *outgoing* ones (limiting absorption principle), where the outgoing wave is the one traveling  
541 towards the corners (as reference to their names). Observed peaks then correspond to attenu-  
attenuated black-hole waves going towards the corners. Similarly, Poynting fluxes get *smoothed out*

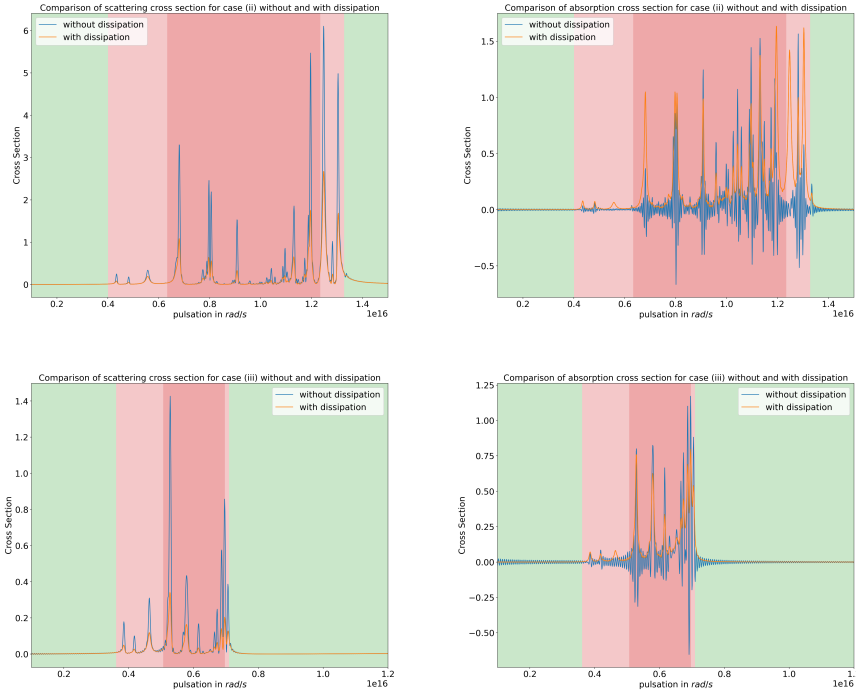


Figure 16: Comparison of cross sections for cases (ii) (top row) - (iii) (bottom row) with and without dissipation: scattering  $C_{sca}$  (left), absorption  $C_{abs}$  (right).

542  
543 by dissipation, and most of the energy fluxes come from the corners at critical pulsations: this  
544 corresponds to *attenuated* black-hole resonances contributions.

545 **Remark 12.** *As explained in Section 3.1, the frequency theory also allows to characterize the*  
546 *singularities as odd or even coupled plasmons depending on the surface plasmon frequency. Due*  
547 *to the chosen non symmetric configuration, we expect that the excitation of odd plasmons will be*  
548 *favoured under the surface plasmon frequency, whereas the excitation of even plasmons will be*  
549 *favoured above the surface plasmon frequency. One can identify a change of behavior in  $C_{sca}$ ,*  
550 *where the scattering cross section vanishes for  $\omega = \omega_{sp}$ .*

551 To sum up, studying the limit non lossy models allows to explain underlying resonances from  
552 physical lossy configurations.

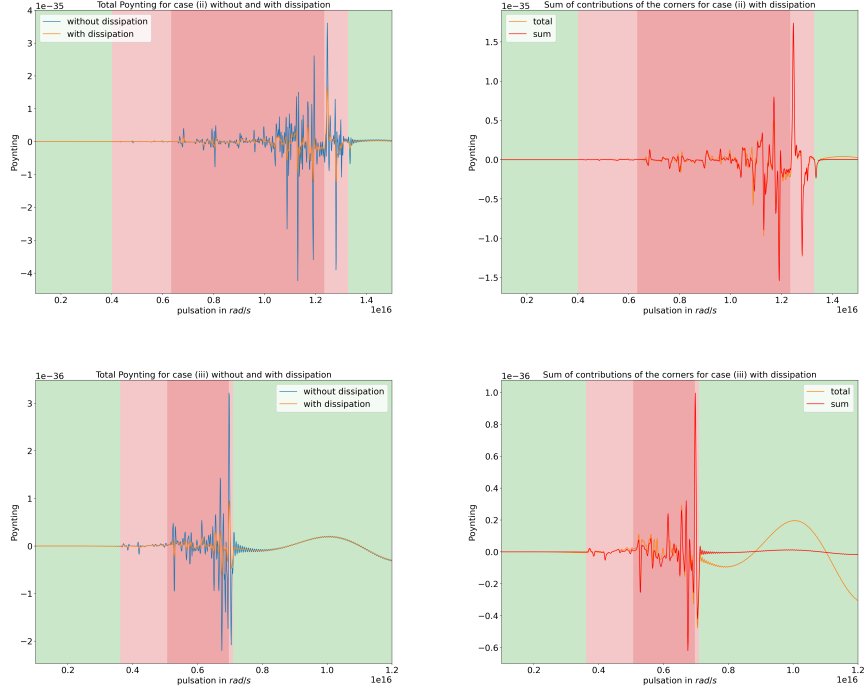


Figure 17: Left: comparison of Poynting fluxes with and without dissipation: case (ii) (top row), case (iii) (bottom row). Right: comparison of total Poynting fluxes and the sum of the Poynting fluxes at the corners: case (ii) with dissipation (top row), case (iii) with dissipation (bottom row).

### 553 5.3. Corner effects

554 It is well known via Mie theory that dissipative subwavelength cylindrical scatterers exhibit  
 555 one resonance located at the surface plasmons frequency  $\omega_{sp}$ . This resonance is called a dipole  
 556 resonance. This result is in accordance with the fact that the critical interval reduces to exactly  
 557  $\{\omega_{sp}\}$  for smooth interfaces. We simply provide below illustrations of the above statement, using  
 558 the same material properties and for  $\mathbb{D}$  a disk with same perimeter as the considered triangle.  
 559 Figure 18 shows that only one resonance at  $\omega_{sp}$  is observed. This also allows to additionally  
 560 validate our approach by recovering a known result.

561 On the other hand, from Section 5.2 we identify multiple resonances at critical pulsations,  
 562 and those resonances are related to specific surface plasmons (called in the limit case black-hole  
 563 waves). In other words, this single subwavelength structure with corners allows to produce mul-  
 564 tipolar resonances (quadripolar, octopolar, etc...). Furthermore, the level of intensity of these  
 565 multiple resonances is equivalent to the level of the dipolar resonance that could be obtained  
 566 with a cylinder with equivalent section perimeter (see Figure 19). The resonance obtained with  
 567 a cylinder is however broader. Thus, it is possible to use triangular scatterers rather than circular  
 568 ones to obtain: (i) multiple resonances with one single structure, (ii) sharper resonances of equiv-  
 569 alent intensity than the single dipolar resonance of a cylindrical structure of equivalent perimeter.  
 570 Polygonal interfaces then offer a larger range of possible light enhancements.

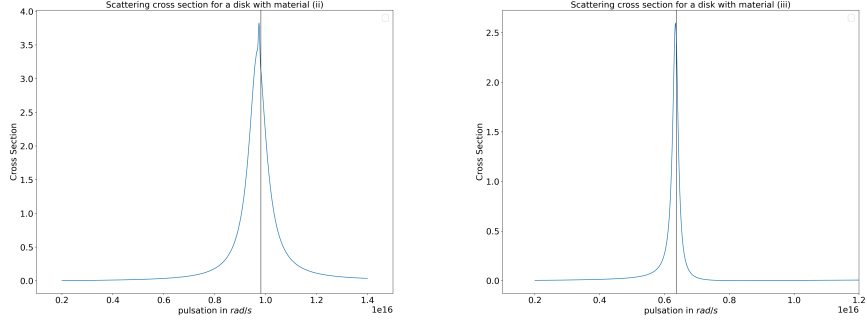


Figure 18: Scattering cross sections for a disk made of a Drude material (ii) and (iii) (no dissipation). The 2D section of the cylinder (a disk) has the same perimeter as the triangle section used in this work. The maximum is achieved at  $\omega = 9.74 \times 10^{15} \text{rad.s}^{-1}$  for case (ii) (0.6% relative error to  $\omega_{sp}$ ) and  $\omega = 6.34 \times 10^{15} \text{rad.s}^{-1}$  for case (iii) (0.5% relative error to  $\omega_{sp}$ ).

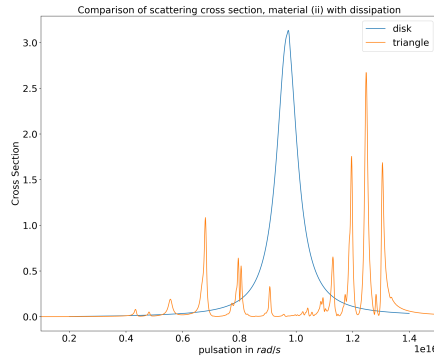


Figure 19: Comparison of scattering cross sections for a disk made of a Drude material (ii) with dissipation using the triangular section and a disk section with same perimeter as the triangle section.

## 571 6. Conclusion

572 In this paper we provided a systematic numerical approach to identify if the limiting ampli-  
 573 tude principle holds in ideal plasmonic structures that is, non lossy plasmonic structures with  
 574 corners, and identified the underlying causes when it does not. Moreover, a study of cross sec-  
 575 tions and Poynting fluxes revealed that the underlying resonances appearing at critical pulsations  
 576 are related to localized surface plasmons at the corners called black-hole waves. We found that  
 577 those characterized behaviors are intrinsic to the problem, as being captured with or without  
 578 dissipation. Overall, this first work provides an interesting framework to investigate unexplored  
 579 models and configurations, where no theory is available. One can for example now investigate  
 580 the fully three-dimensional case, where the associated critical interval is not explicitly known  
 581 in general, and test other plasmonic models such as Drude-Lorentz or more generalized models  
 582 (such as those in [31]). In particular, future work will include the study of non-local effects.

583 **Acknowledgment**

584 CC acknowledges support by the National Science Foundation Grant: DMS-2009366.

585

586 **References**

- 587 [1] S. Maier, *Plasmonics - Fundamentals and applications*, Springer, 2007.
- 588 [2] W. Barnes, A. Dereux, T. Ebbesen, Surface plasmon subwavelength optics, *Nature* 424 (6950) (2003) 824–830.
- 589 [3] A. Zayats, I. Smolyaninov, A. Maradudin, Nano-optics of surface plasmon polaritons, *Physics Reports* 408 (3–4)
- 590 (2005) 131–314.
- 591 [4] T. Sannomiya, C. Hafner, J. Voros, In situ sensing of single binding events by localized surface plasmon resonance,
- 592 *Nano Letters* 8 (10) (2008) 3450–3455.
- 593 [5] K. Mayer, S. Lee, H. Liao, B. Rostro, A. Fuentes, P. Scully, C. Nehl, J. Hafner, A label-free immunoassay based
- 594 upon localized surface plasmon resonance of gold nanorods, *ACS Nano* 2 (4) (2008) 687–692.
- 595 [6] L. Novotny, N. Van Hulst, Antennas for light, *Nature photonics* 5 (2) (2011) 83–90.
- 596 [7] G. Akselrod, C. Argyropoulos, T. Hoang, C. Ciraci, C. Fang, J. Huang, D. Smith, M. Mikkelsen, Probing the
- 597 mechanisms of large purcell enhancement in plasmonic nanoantennas, *Nature Photonics* 8 (11) (2014) 835–840.
- 598 [8] P. Drude, Zur elektronentheorie der metalle, *Annalen der Physik* 306 (1900) 566–613.
- 599 [9] C. Morawetz, The limiting amplitude principle, *Communications on Pure and Applied Mathematics* 15 (1962)
- 600 349–361.
- 601 [10] N. Iwasaki, On the principle of limiting amplitude, *Publications of the Research Institute for Mathematical Sciences*
- 602 3 (1968) 373–392.
- 603 [11] D. Eidus, The principle of limit amplitude, *Russ. Math. Surv.* 24 (1969) 97–167.
- 604 [12] G. Kriegsmann, Exploiting the limiting amplitude principle to numerically solve scattering problems, *Wave Motion*
- 605 4 (1982) 371–380.
- 606 [13] G. Roach, B. Zhang, The limiting-amplitude principle for the wave propagation problem with two unbounded
- 607 media, *Math. Proc. Camp. Phil. Soc.* 112 (1992) 207–223.
- 608 [14] B. Gralak, A. Tip, Macroscopic Maxwell’s equations and negative index materials, *Journal of Mathematical Physics*
- 609 5 (2010) 052902.
- 610 [15] M. Cassier, Analysis of two wave propagation phenomena: 1) space–time focusing in acoustics; 2) transmission
- 611 between a dielectric and a metamaterial., Ph.D. thesis, École Polytechnique (2014).
- 612 [16] A.-S. Bonnet-Ben Dhia, L. Chesnel, P. Ciarlet Jr.,  $T$ -coercivity for scalar interface problems between dielectrics
- 613 and metamaterials, *Math. Model. Numer. Anal.* 46 (06) (2012) 1363–1387.
- 614 [17] A.-S. Bonnet-Ben Dhia, L. Chesnel, P. Ciarlet Jr.,  $T$ -coercivity for the Maxwell problem with sign-changing coef-
- 615 ficients, *Communications in Partial Differential Equations* 39 (6) (2014) 1007–1031.
- 616 [18] H. Kettunen, L. Chesnel, H. Hakula, H. Wallén, A. Sihvola, Surface plasmon resonances on cones and wedges, in:
- 617 2014 8th International Congress on Advanced Electromagnetic Materials in Microwaves and Optics, IEEE, 2014,
- 618 pp. 163–165.
- 619 [19] H.-M. Nguyen, Limiting absorption principle and well-posedness for the Helmholtz equation with sign changing
- 620 coefficients, *Journal de Mathématiques Pures et Appliquées* 106 (2) (2016) 342–374.
- 621 [20] A.-S. Bonnet-Ben Dhia, C. Carvalho, L. Chesnel, P. Ciarlet Jr., On the use of perfectly matched layers at corners
- 622 for scattering problems with sign-changing coefficients, *J. Comput. Phys.* 322 (2016) 224–247.
- 623 [21] A.-S. Bonnet-Ben Dhia, L. Chesnel, M. Rihani, Maxwell’s equations with hypersingularities at a conical plasmonic
- 624 tip, arXiv preprint arXiv:2010.08472 (2020).
- 625 [22] C. Carvalho, Z. Moitier, Asymptotics for metamaterial cavities and their effect on scattering, arXiv preprint
- 626 arXiv:2010.07583 (2020).
- 627 [23] M. Cassier, P. Joly, M. Kachanovska, Mathematical models for dispersive electromagnetic waves: An overview,
- 628 *Comput. and Math. with Appl.* 74 (2017) 2792–2830.
- 629 [24] S. Nicaise, Stabilization of a Drude/vacuum Model, *Zeitschrift für Analysis und ihre Anwendungen* 37 (2018)
- 630 349–375.
- 631 [25] A.-S. Bonnet-Ben Dhia, P. Ciarlet Jr., C. Zwölf, Time harmonic wave diffraction problems in materials with
- 632 sign-shifting coefficients, *J. Comput. Appl. Math.* 234 (2010) 1912–1919, corrigendum *J. Comput. Appl. Math.*,
- 633 234:2616, 2010.
- 634 [26] A.-S. Bonnet-Ben Dhia, L. Chesnel, X. Claeys, Radiation condition for a non-smooth interface between a dielectric
- 635 and a metamaterial, *Math. Models Meth. App. Sci.* 23 (09) (2013) 1629–1662.
- 636 [27] F. Frezza, F. Mangini, N. Tedeschi, Introduction to electromagnetic scattering: tutorial, *JOSA A* 35 (1) (2018).

- 637 [28] A.-S. Bonnet-Ben Dhia, C. Carvalho, P. Ciarlet Jr., Mesh requirements for the finite element approximation of  
638 problems with sign-changing coefficients, *Numerische Mathematik* 138 (4) (2018) 801–838.
- 639 [29] V. Vinoles, Regularity results for transmission problems with sign-changing coefficients: a modal approach, arXiv  
640 preprint arXiv:1611.00304 (2016).
- 641 [30] P. B. Johnson, R. W. Christy, Optical constants of the noble metals, *Physical Review B* 6 (1972) 4370–4379.
- 642 [31] S. Lanteri, C. Scheid, J. Viquerat, Analysis of a generalized dispersive model coupled to a DGTD method with  
643 application to nanophotonics, *SIAM J. Sci. Comput.* 39 (3) (2017) A831–A859.
- 644 [32] K. Busch, M. König, J. Niegemann, Discontinuous Galerkin methods in nanophotonics, *Laser and Photonics Re-*  
645 *views* 5 (2011) 1–37.
- 646 [33] S. Descombes, C. Durochat, S. Lanteri, L. Moya, C. Scheid, J. Viquerat, Recent advances on a DGTD method  
647 for time-domain electromagnetics, *Photonics and Nanostructures-Fundamentals and Applications* 11 (4) (2013)  
648 291–302.
- 649 [34] S. Lanteri, C. Scheid, Convergence of a discontinuous Galerkin scheme for the mixed time domain Maxwell’s  
650 equations in dispersive media, *IMA J. Numer. Anal.* 33 (2) (2013) 432–459.
- 651 [35] N. Schmitt, C. Scheid, S. Lanteri, J. Viquerat, A. Moreau, A DGTD method for the numerical modeling of the  
652 interaction of light with nanometer scale metallic structures taking into account non-local dispersion effects, *J.*  
653 *Comput. Phys.* 316 (2016) 396–415.
- 654 [36] L. Chesnel, Investigation of some transmission problems with sign-changing coefficients. application to metamate-  
655 rials, Ph.D. thesis, École Polytechnique (2012).